

# Direct Collapse to Supermassive Black Hole Seeds: Comparing the AMR and SPH Approaches

Yang Luo<sup>1\*</sup>, Kentaro Nagamine<sup>1,2†</sup>, Isaac Shlosman<sup>3,1‡</sup>

<sup>1</sup> *Theoretical Astrophysics, Department of Earth & Space Science, Osaka University, 1-1 Machikaneyama, Toyonaka, Osaka 560-0043, Japan*

<sup>2</sup> *Department of Physics & Astronomy, University of Nevada Las Vegas, 4505 S. Maryland Pkwy, Las Vegas, NV 89154-4002, USA*

<sup>3</sup> *Department of Physics & Astronomy, University of Kentucky, Lexington, KY 40506-0055, USA*

Accepted ?; Received ??; in original form ???

## ABSTRACT

We provide detailed comparison between the AMR code Enzo-2.4 and the SPH/ $N$ -body code GADGET-3 in the context of isolated or cosmological direct baryonic collapse within dark matter (DM) halos to form supermassive black holes. Gas flow is examined by following evolution of basic parameters of accretion flows. Both codes show an overall agreement in the general features of the collapse, however, many subtle differences exist. For isolated models, the codes increase their spatial and mass resolutions at different pace, which leads to substantially earlier collapse in SPH than in AMR cases due to higher gravitational resolution in GADGET-3. In cosmological runs, the AMR develops a slightly higher baryonic resolution than SPH during halo growth via cold accretion permeated by mergers. Still, both codes agree in the buildup of DM and baryonic structures. However, with the onset of collapse, this difference in mass and spatial resolution is amplified, so evolution of SPH models begins to lag behind. Such a delay can have effect on formation/destruction rate of  $\text{H}_2$  due to UV background, and on basic properties of host halos. Finally, isolated non-cosmological models in spinning halos, with spin parameter  $\lambda \sim 0.01 - 0.07$ , show delayed collapse for greater  $\lambda$ , but pace of this increase is faster for AMR. Within our simulation setup, GADGET-3 requires significantly larger computational resources than Enzo-2.4 during collapse, and needs similar resources, during the pre-collapse, cosmological structure formation phase. Yet it benefits from substantially higher gravitational force and hydrodynamic resolutions, except at the end of collapse.

**Key words:** methods: numerical — galaxies: formation — galaxies: high-redshift — cosmology: theory — cosmology: dark ages, reionization, first stars

## 1 INTRODUCTION

The origin of supermassive black holes (SMBHs) in the galactic centers remains an unresolved problem in astrophysics. Unless the SMBHs are primordial, a number of alternative scenarios exists. First, they could grow from relics of the Population III stars (e.g., Madau & Rees 2001; Abel et al. 2002; Bromm & Larson 2004; Volonteri & Rees 2005) — the largely pre-galactic objects whose masses appear to be comparable or slightly higher than normal OB stars (e.g., Turk et al. 2009; Hosokawa et al. 2011; Wise et al. 2012; Hirano et al. 2014; Fraser et al. 2015, see also Bromm 2013 for review). Second, they could form from the runaway collapse

of compact stellar clusters, subject to general relativistic effects (e.g., Zel’dovich & Podurets 1965; Shapiro & Teukolsky 1985), or stellar/gasdynamics evolution of stellar clusters (e.g., Begelman & Rees 1978). Most appealing, however, is the third alternative which involves a direct baryonic collapse to form massive black hole seeds of  $\sim 10^4 - 10^7 M_\odot$ , (e.g., Haehnelt & Rees 1993; Loeb & Rasio 1994; Bromm & Loeb 2003; Koushiappas et al. 2004; Begelman et al. 2006; Volonteri & Rees 2006; Begelman et al. 2008; Begelman & Shlosman 2009; Milosavljević et al. 2009; Mayer et al. 2010; Schleicher et al. 2010; Johnson et al. 2011; Choi et al. 2013, 2015; Latif et al. 2013; Prieto et al. 2013; Shlosman et al. 2016) which experience a substantial growth subsequently. Depending on the chemical composition of the collapsing gas, this can take place when suitable dark matter (DM) halos appear in the universe. For a primordial composition, hydrogen can be either atomic, with a cooling floor of just

\* E-mail: yluo@vega.ess.sci.osaka-u.ac.jp

† E-mail: kn@vega.ess.sci.osaka-u.ac.jp

‡ E-mail: shlosman@pa.uky.edu

below  $10^4$  K, or molecular, which is able to cool down by additional  $\sim 2$  orders of magnitude. In the former case, for the gas to collapse, the virial temperature of DM halos must exceed the cooling floor of hydrogen, with the corresponding mass of  $\sim 10^8 M_\odot$ . In the latter case, the critical halo masses will be smaller.

Direct collapse scenario involves gravitational collapse from typical spatial scales of  $\sim 1$  kpc, down to  $\sim 1 - 100$  Schwarzschild radii of the seed SMBH — an enormous dynamic range. Solution of the full problem requires application of the coupled radiative hydrodynamics of the collapsing matter, MHD, and other ingredients, and cannot be accomplished analytically. Here we limit ourselves to the hydrodynamical and radiation part of the problem, and, in addition, assume that the collapsing gas is optically-thin to its own produced radiation. The heavily computational approach employed by various groups to address this and related issues involves different numerical algorithms. These include the adaptive mesh refinement (AMR) and Smooth Particle Hydrodynamics (SPH) codes, which are semi-Eulerian and Lagrangian, respectively. In this work, we compare the efficiency and reliability of two representative codes, Enzo-2.4 AMR code (Bryan & Norman 1997; Norman & Bryan 1999; Bryan et al. 2014a), and modified version of GADGET-3 SPH/ $N$ -body code (Springel 2005).

Previous comparison between the grid and Lagrangian codes have both achieved results within  $\sim 20\%$ , in the cosmological context (e.g., O’Shea et al. 2005), and also found significant differences. One of the primary results that they found was that the AMR requires significantly greater computational resources in order to achieve the same DM halo mass function as in the SPH code. This was due to the lower force resolution in the AMR code at early times than in SPH code, which resulted in the lack of early growth of density perturbations at high redshifts.

In the Santa Barbara Cluster Comparison project (Frenk et al. 1999), different groups have simulated formation of one galaxy cluster from identical initial conditions. In this case, for example, the central entropy profile (within the virial radius) presents a floor in grid codes, whereas such feature is absent in the SPH codes. These discrepancies remain largely unexplained although more recent works have improved significantly the agreement by using the entropy-conserving version of SPH codes (e.g., Springel & Hernquist 2003; Ascasibar et al. 2003; Vogelsberger et al. 2012). The ongoing AGORA project of a broad comparison between a number of grid and Lagrangian codes of well-resolved galaxies focuses on convergence study of various feedback processes (Kim et al. 2014). However this comparison project is in its early stage.

Statistics of driven, supersonic turbulence at a high Mach number have been performed by Price & Federrath (2010) using FLASH, a widely used Eulerian grid-based AMR code, and the SPH code PHANTOM. Excellent agreement between these codes has been found at similar number of particles and grid cells for the basic statistical properties of the turbulence, such as the slope in the velocity power spectrum, lognormal probability distribution function (PDF), the width of the PDF, etc. At the same time, SPH code has shown a better spatial resolution. Dense structures have been resolved already with  $128^3$  SPH particles, compared to  $512^3$  cells required for the same purpose in

AMR. Unfortunately, this comparison differs fundamentally from the one performed in the present work: it is entirely non-gravitational. As a result, the density stratification was much weaker than one observes during gravitational collapse, and hence the evolution in their simulation did not go as far as in our current work.

It remains unclear, whether SPH or AMR codes are more accurate in general simulation regimes. Both methods have their shortcomings. For example, in AMR, if the fluid moves rapidly across the mesh, the truncation errors lead to significant departure from the same simulation if there is no bulk velocity (Tasker et al. 2008). Hopkins (2013) have studied a number of SPH modifications, in particular alternative SPH equations of motion that guarantee conservation and improved treatment of fluid contact discontinuities (e.g., Kelvin-Helmholtz instability). Good agreement has been reported for supersonic flows and associated strong shocks, but the SPH suppresses mixing in subsonic, thermal pressure-dominated regimes. Saitoh & Makino (2013) have also provided a new density-independent formulation of SPH which removes the artificial surface tension. Their method was more formally treated in the Lagrangian formalism by Hopkins (2013).

Another important issue for classical AMR codes is the angular momentum conservation. Unless we can anticipate the geometry of the flow and adjust accordingly the mesh so that the fluid velocity is perpendicular to the boundary, the accuracy is seriously compromised and subject to artificially enhanced diffusion. Finally, the refinement criteria is somewhat arbitrary and can produce various artefacts. At the refinement boundaries, there is a significant loss of accuracy as the refinement is necessarily discontinuous.

On the other hand, the SPH in 3-D suffers from a poor shock resolution, noise on the scale of the smoothing kernel, and low-order accuracy for the treatment of contact discontinuities. Hydrodynamic instabilities like the Kelvin-Helmholtz can be suppressed (Agertz et al. 2007), although recent modifications put forth by Hopkins (2013) has been claimed to correct these problems. In real fluids, the entropy is raised in shocks because particle collisions randomize their velocities which increase the heat and the entropy. The SPH does not capture shocks properly because entropy must be generated locally to dissipate the small scale velocities. In order to mimic this process, and to prevent interpenetration of the SPH particles at the shock locations, artificial viscosity is required. The introduction of the latter usually results in an overly viscous fluid away from shocked regions. To overcome this, the Balsara (1995) switch or Cullen & Dehnen (2010) formulation have been developed.

The aim of this paper is to compare the ability of AMR and SPH codes in following the direct collapse of gas with a primordial composition, i.e., involving identical atomic hydrogen cooling. We compute and analyze models of gas collapse inside DM halos in isolated and cosmological settings. Our models span more than 7 orders of magnitude in radius, from 1 kpc down to  $10^{-4}$  pc. Of course, the main question is whether both codes can describe the evolution that leads to the same end product. However, specific details are important as well, namely, are various physical quantities (e.g., gas density, temperature, tangential and radial velocity, and angular momentum distributions) similar at various times of the collapse? Does it take the same time to collapse, and

how do accretion rates and their temporal and radial distributions compare?

This paper is structured as follows. In Section 2, we briefly describe the AMR and SPH codes used. Section 3 provides the results of our comparison runs, and in the last section, we discuss our results and summarize them.

## 2 NUMERICAL TECHNIQUES

### 2.1 Enzo AMR and GADGET-3 SPH

The AMR code Enzo-2.4 has been tested extensively and is publicly available. It uses a multi-grid particle-mesh  $N$ -body method to calculate the gravitational dynamics, including collisionless DM particles, and a second-order piecewise parabolic method (PPM, Colella & Woodward 1984; Bryan et al. 1995) to solve hydrodynamics. ZEUS hydro is also available, but we use PPM here.

The structured AMR used in Enzo places no fundamental restrictions on the number of rectangular grids used to cover some region of space at a given level of refinement, or on a number of refinement levels (Berger & Colella 1989). A grid is refined by a factor of 2 in lengthscale, if either the gas or DM density become greater than  $\rho_0 N^\ell$ , where  $\rho_0$  is the cosmic mean density for the gas or DM, respectively. The refinement factor is  $N = 2$ , and  $\ell$  refers to the AMR refinement level.

The Jeans length has been resolved by at least 4 cells in these simulations to satisfy the Truelove et al. (1997) requirement for resolution. For the SPH code, an equivalent criterion is to resolve the local Jeans mass by having at least twice the number of particles in an SPH kernel (Bate & Burkert 1997).

In GADGET-3, the gas and the DM are represented by particles. The  $N$ -body solver is essentially the same as in GADGET-2 (Springel 2005), with some improvements for optimization purposes, such as the domain decomposition. To achieve the spatial adaptivity at a moderate computational cost, it uses a hierarchical multipole expansion, i.e., the tree algorithm (Barnes & Hut 1986). The gravitational potential is softened below a spatial scale specified by the gravitational softening length. In principle, this kernel (and the associated softening length,  $\epsilon$ , which represents the force resolution) can differ from the smoothing length used in the hydrodynamical method, as we describe below. But mostly the SPH uses the same cubic-spline kernel, with a fixed  $\epsilon$  evaluated as the mean initial interparticle distance, divided by a fudge factor of  $\sim 20 - 30$ .

We use GADGET-3 with the density-independent SPH version with a quintic kernel and time-independent viscosity (Hopkins 2013). Comparison of various viscosity algorithms has been performed by Cullen & Dehnen (2010), who proposed a new artificial viscosity prescription. This viscosity grows rapidly in strong shocks, and decays rapidly away from the shocks to a minimum  $\alpha = 0.2$ , compared to usual constant artificial viscosity. With this method, the gas becomes virtually inviscid away from the shocks, while maintaining particle order. The viscosity decay length is taken as 3.73, and the source scaling equal to 2.77.

For the cooling package, we use Grackle version 2.0 for GADGET-3, and Grackle version 1.1 for Enzo. These ver-

sions for the SPH and AMR codes have identical chemistry and cooling (Bryan et al. 2014b; Kim et al. 2014, <https://grackle.readthedocs.org/>). This library was born out of the chemistry and cooling routines of the Enzo simulation code. The Grackle solves for radiative cooling and internal energy, calculates cooling time, temperature, pressure, and ratio of specific heats. It uses a non-equilibrium primordial chemistry network for atomic H and He (Abel et al. 1997; Anninos et al. 1997),  $H_2$  and HD, Compton cooling off the cosmic microwave background, tabulated metal cooling and photo-heating rates calculated with Cloudy (Ferland et al. 2013). In addition, Grackle provides a look-up table for equilibrium cooling. The gas is assumed to be dust-free and optically-thin and the metals are assumed to be in ionization equilibrium. The cooling rate for a parcel of gas with a given density, temperature, and metallicity, that is photoionized by incident radiation of known spectral shape and intensity can be pre-calculated. As we focus on gravitational collapse models at  $z > 10$ , and limit the runs to the optically-thin regime, the UV background is not included, and we neglect the radiative transfer of ionizing photons in the present work.

### 2.2 Setup in Isolated Models

For isolated models, we adopt the WMAP5 cosmological parameters (Komatsu et al. 2009), namely,  $\Omega_m = 0.279$ ,  $\Omega_b = 0.0445$ ,  $h = 0.701$ , where  $h$  is the Hubble constant in units of  $100 \text{ km s}^{-1} \text{ Mpc}^{-1}$ . We set up the details of an isolated DM halo that is consistent with the cosmological context that we work with. Therefore, some of the halo parameters are specified with units that include the Hubble parameter, although we use physical quantities (not comoving) in all isolated case calculations. In both codes, we define a DM halo as having the density equal to the critical density  $\Delta_c$  times the mean density of the universe,  $\rho_b$ , which depends on the redshift  $z$  and the cosmological model. The top-hat model is used to calculate  $\Delta_c(z)$ , and the density is calculated within a virial radius,  $R_{\text{vir}}$ . The halo virial mass is  $M_{\text{vir}}(z) = (4\pi/3)\Delta_c(z)\rho_b R_{\text{vir}}$ .

For isolated models we work in physical coordinates. We assume that the gas fraction in the model is equal to the universal ratio, and simulate the gas evolution within DM halos of a virial mass of  $M_{\text{vir}} = 2 \times 10^8 h^{-1} M_\odot$  and a virial radius  $R_{\text{vir}} = 945 h^{-1} \text{ pc}$ . The initial temperature of the gas is taken to be  $T = 3.2 \times 10^4 \text{ K}$ . The simulation domain is a box with a size  $L_{\text{box}} = 6 \text{ kpc}$  centered on the halo. In the following, we abbreviate the spherical radii with  $R$  and cylindrical ones with  $r$ .

The initial DM and gas density profiles  $\rho_{\text{DM}}(R)$  and  $\rho_g(R)$  are those of an nonsingular isothermal spheres with a flat density core of  $R_{\text{c,DM}} = 0.34 \text{ pc}$  for DM and  $R_{\text{c,g}} = 142.65 \text{ pc}$  for the gas, respectively (Fig. 1):

$$\rho_g(R) = \rho_{g,0} \begin{cases} \frac{1}{(1 + \frac{R}{R_{\text{c,g}}})^2} & (R \leq R_{\text{vir}}) \\ \frac{1}{(1 + \frac{R_{\text{vir}}}{R_{\text{c,g}}})^2} \frac{R_{\text{vir}}^3}{R^3} & (R > R_{\text{vir}}), \end{cases} \quad (1)$$

$$\rho_{\text{DM}}(R) = \rho_{\text{DM},0} \frac{R_{\text{c,DM}}^2}{R^2} \quad (R \leq R_{\text{vir}}), \quad (2)$$

where  $\rho_{\text{DM},0} = 7.38 \times 10^{-18} \text{ g cm}^{-3}$ , and  $\rho_{g,0} = 1.66 \times$

**Table 1.** Simulation parameters for the isolated halo models with Enzo AMR and GADGET-3 SPH. Name of the run and the values of spin parameter  $\lambda$  is listed. “I” in the model abbreviation stands for isolated runs, and the number  $\lambda \times 100$  for DM halos. Cosmological models (not shown in the Table), are abbreviated by “C” and by  $\lambda \times 100$ .

| Name: isolated | $\lambda$ |
|----------------|-----------|
| AMR-I1         | 0.01      |
| AMR-I3         | 0.03      |
| AMR-I5         | 0.05      |
| AMR-I7         | 0.07      |
| SPH-I1         | 0.01      |
| SPH-I3         | 0.03      |
| SPH-I5         | 0.05      |
| SPH-I7         | 0.07      |

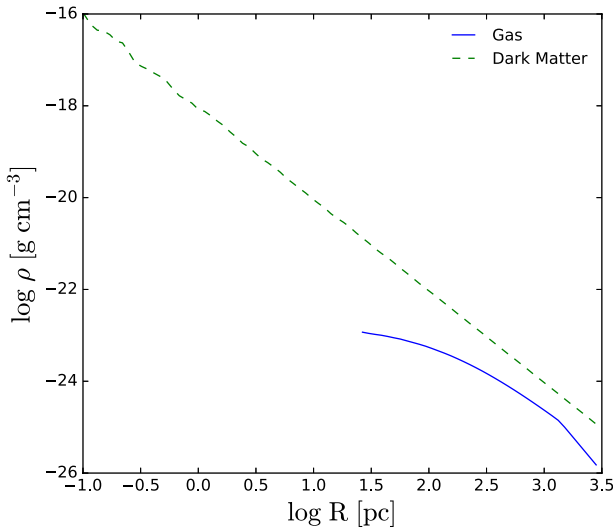


**Figure 1.** Initial density profiles in the isolated halo model for the gas (solid line) and DM (dashed line) as a function of radius.

$10^{-23} \text{ g cm}^{-3}$ . Such DM halos are similar to the NFW halos (Navarro et al. 1997), and are simple to construct. The DM halo core size is actually set by the gravitational softening length for GADGET-3 SPH.

The DM halo rotation is defined in terms of the cosmological spin parameter  $\lambda$ ,

$$\lambda = \frac{J}{\sqrt{2} M_{\text{vir}} R_{\text{vir}} v_c} \quad (3)$$

where  $J$  is the total angular momentum of the DM halo,  $M_{\text{vir}}$  the halo virial mass, and  $v_c$  the circular velocity at  $R_{\text{vir}}$ , which is constant with radius for an isothermal sphere mass distribution. The mean DM spin is  $\lambda \sim 0.035 \pm 0.005$  (e.g., Bullock et al. 2001). We explore the range of  $\lambda \simeq 0 - 0.07$  in our isolated models. For identical  $\lambda$ , we sample the same initial density distribution using four different random number sequences. The properties of the collapsing baryons have been averaged over these sequences. Models having identical mass distribution and differing only in the initial random sequence, are abbreviated similarly.

To produce the DM halos with a pre-specified  $\lambda$  for iso-

lated halo models, we follow the the prescription of Long et al. (2014). In short, we set the isotropic distribution of velocity dispersion in DM. Then reverse tangential velocities for a fraction of DM particles to reproduce the specific angular momentum described above, with  $\lambda$  equal to the required value. For both SPH particles and the gas in AMR grid cells, we calculate the average tangential velocities of the background DM in cylindrical shells, accounting for the dependence along the (rotation)  $z$ -axis. The rotational velocities for the gas in the equatorial plane of the DM halo are given by

$$v_t(r) = v_0 \times \begin{cases} r/R_{c,g} & \text{if } r \leq R_{c,g}, \\ 1 & \text{if } R_{c,g} \leq r \leq R_{\text{vir}}, \end{cases} \quad (4)$$

where  $v_0$  is tangential velocity defined by  $\lambda$ . The radial velocity dispersion in the center is given by  $\sigma = \sqrt{GM_{\text{vir}}/2R_{\text{vir}}} = 21.3 \text{ km s}^{-1}$ , where  $G$  is the gravitational constant. The isolated halo models have been listed in Table 1 and are identified with “I” and the value of the spin parameter multiplied by 100. In cosmological models, we use the same notation, but replace “I” with “C”.

In the isolated models of GADGET-3, the DM resolution is set by the fixed gravitational softening length,  $\epsilon_{\text{DM}} = 0.37 \text{ pc}$ . This is done in order to match the condition in Enzo runs. For Enzo, it corresponds to an initial root grid of  $64^3$  in a 6 kpc region with a maximal refinement level of 8 allowed for gravity,  $\epsilon_{\text{DM,min}} = 6000/64/2^8 = 0.37 \text{ pc}$ .

For the gas, the gravitational softening is  $\epsilon_g = 10^{-4} \text{ pc}$ , which is a fixed number for GADGET-3 and serves as a minimal value for Enzo. In other words, we use the initial resolution of  $512^3$  SPH particles or cells for baryons, and  $100^3$  particles or particles-in-mesh for the DM. All other parameters in Enzo and GADGET-3 runs are similar. The force resolution in adaptive PM codes is twice the minimal cell size (e.g., Kravtsov et al. 1997). Isolated and cosmological runs and their parameters are summarized in Tables 1 and 2. We use the models AMR-I5 and SPH-I5 as representative isolated models.

### 2.3 Setup in Cosmological Models

For further comparison, we use zoom-in cosmological simulations with the same composition as in isolated models to follow up the gas evolution within DM halos. The initial conditions (ICs) are generated using WMAP5 cosmology:  $\Omega_\Lambda = 0.721$ ,  $\Omega_m = 0.279$ ,  $\Omega_b = 0.0445$ ,  $h = 0.701$ ,  $\sigma_8 = 0.807$ , and  $n = 0.961$ . The models run from  $z = 200$ . The same cooling packages have been used for cosmological models as for isolated ones (Section 2.1).

For the initial setup, we use the MUSIC algorithm (Hahn & Abel 2011) to generate cosmological zoom-in ICs. MUSIC uses a real-space convolution approach in conjunction with an adaptive multi-grid Poisson solver to generate highly accurate nested density, particle displacement, and velocity fields suitable for multi-scale zoom-in simulations of structure formation in the universe.

Generating a set of zoom-in ICs is a two-step process. First, we generate  $3h^{-1} \text{ Mpc}$  comoving  $256^3$  DM-only ICs for the pathfinder simulation and run it without AMR until  $z = 10$ . Using the HOP group finder (Eisenstein & Hut 1998), we select an appropriate DM halo, whose mass is  $\gtrsim 10^8 h^{-1} M_\odot$  at  $z = 10$ . Second, we generate  $0.4h^{-1} \text{ Mpc}$

**Table 2.** Summary of simulation setup for Enzo-2.4 (AMR) and GADGET-3 (SPH) simulations.

| Parameters                                       | Isolated model   | Cosmological model   |
|--|--|--|
| Simulation Volume                                | 6 kpc box  | $3h^{-1}$ Mpc with a zoom-in region of $0.4h^{-1}$ Mpc   |
| Initial baryonic resolution                      | $64^3$ root-grid with 3 levels of refinement;<br>Effective $512^3$ zoom grid and SPH particles   | $256^3$ root-grid and SPH particles;<br>Effective $2048^3$ zoom grid and SPH particles   |
| Number of DM particles                           | $100^3$  | $256^3$ for outer region;<br>Effective $2048^3$ for zoom region <sup>†</sup>   |
| Mass resolution                                  | $532.5 M_{\odot}$ for DM particles<br>$0.7 M_{\odot}$ for gas particles  | $245.7 h^{-1} M_{\odot}$ for DM particles<br>$44.7 h^{-1} M_{\odot}$ for gas particles   |
| Gravitational softening                          | $\epsilon_{\text{DM,min}} = 0.37 \text{ pc}$ for DM in Enzo <sup>#</sup><br>$\epsilon_{\text{DM}} = 0.37 \text{ pc}$ for DM in GADGET<br>$\epsilon_{\text{g,min}} = \text{smallest cell size for gas in Enzo}$<br>$\epsilon_{\text{g}} = 10^{-4} \text{ pc}$ for gas in GADGET | $\epsilon_{\text{DM,min}} = 0.36 h^{-1} \text{ pc}$ for DM in Enzo <sup>##</sup><br>$\epsilon_{\text{DM}} = 0.36 h^{-1} \text{ pc}$ for DM in GADGET<br>$\epsilon_{\text{g,min}} = \text{smallest cell size for gas in Enzo}$<br>$\epsilon_{\text{g}} = 10^{-3} h^{-1} \text{ pc}$ for gas in GADGET |
| Minimum gas smoothing length $\eta_{\text{min}}$ | $10^{-3} \text{ pc}$   | $10^{-2} h^{-1} \text{ pc}$ ###  |

<sup>†</sup> The size of the zoom-in region is about one-tenth of the outer region, therefore the actual grid/particle number in the zoom region is initially  $\sim 200^3$  for both baryons and DM particles.

<sup>#</sup> Maximum refinement level for DM gravity is set to 8 levels for Enzo in isolated models, i.e.,  $\epsilon_{\text{DM,min}} = 6000/64/2^8 = 0.37 \text{ pc}$ . The isolated models do not have Hubble expansion in space, so there is no factor of  $h^{-1}$  and all numbers are physical.

<sup>##</sup> Maximum refinement level for DM gravity is set to 15 levels for Enzo in cosmological models, i.e.,

$$\epsilon_{\text{DM,min}} = 3 \times 10^6 / 256 / 2^{15} = 0.36 h^{-1} \text{ pc}.$$

<sup>###</sup> Maximum refinement levels for the gas in Enzo are set to 17 levels in isolated models and 20 levels in cosmological models.

ICs with  $2048^3$  effective resolution in DM and gas, embedded in the lower resolution outer region. Since we use the same random seeds for these ICs as the first step, the phases of both ICs are identical. The zoom-in region is centered on the selected halo position and is set to be large enough to cover the initial positions of all selected halo particles. We perform the zoom-in procedure for each of the targeted halos.

In the cosmological runs, the gravitational softening is  $10^{-3} \text{ pc}$  in the comoving coordinates, in the SPH run. We have measured the spin parameter of many halos in the range of  $\lambda \sim 0.01 - 0.07$  in our zoom region at  $z \sim 10$ , and use  $\lambda \sim 0.04$  as a representative one for both AMR and SPH runs.

### 3 RESULTS

We aim at comparing results for direct baryonic collapse within DM halos by Enzo-2.4 AMR and GADGET-3 SPH codes. As a first step, we compare the isolated models. The cosmological halos have a range of spin parameter, as discussed in § 2.2. To match the conditions of these halos, we generate isolated halos with the same range of  $\lambda$  (Table 1 and § 3.1). The cosmological halos are examined in § 3.2. Lastly, we test the effect of  $\lambda$  on the dynamics of the collapse in isolated and cosmological models (§§ 3.3, 3.4).

#### 3.1 Direct collapse in isolated models

Direct collapse of isolated models with atomic gas has been performed and analysed by Choi et al. (2013) for  $\lambda = 0.05$ , using Enzo. Many of the aspects of its evolution are generic. We define  $t = 0$  at the start of the run, and stop the run when the central collapse reaches the final resolution of  $R_{\text{fin}} \sim 10^{-3} \text{ pc}$ , in both Enzo and GADGET-3, in order to allow a meaningful comparison, because the SPH run would

have difficulty reaching a higher resolution without invoking complicated procedures, such as SPH particle splitting.

The DM in isolated models has isothermal profiles by construction, i.e.,  $\rho_{\text{DM}} \propto R^{-2}$ . They remain nearly identical to ICs. As the collapse proceeds and reaches the central region, the DM is dragged inward by the gas, and is compressed adiabatically, forming new cusps with slopes  $\sim -1$  to  $\sim -2$ .

The baryonic collapse proceeds in two stages, which are representative for all isolated models. First, the gas cools down to the cooling floor of atomic gas, then collapses following a self-similar solution, analogous to the Larson-Penston solution for an isothermal, self-gravitating gas cloud,  $\rho \propto R^{-2}$  (Larson 1969; Penston 1969). But significant differences are obvious, as angular momentum is present and modifies the solution, and the DM dominates the gravitational potential everywhere during the initial stage.

When collapsing gas reaches the centrifugal barrier, a shock forms, where the density jumps and the radial velocity drops abruptly (top panels of Figure 2). The gas accumulates behind the shock and forms a disk which grows in mass. As the gas density in the inner disk surpasses that of the DM, the 2nd stage of the collapse ensues, and proceeds with an increasingly short timescale. Basically, most of the gas behind the shock collapses and reaches the prescribed resolution of  $\sim 10^{-4} \text{ pc}$  (e.g., Choi et al. 2013), although here we compare the final distributions when  $R_{\text{fin}} \sim 10^{-3} \text{ pc}$  has been reached.

The current AMR simulations with various  $\lambda$  follow basically the same outline. The initial positions of shocks in all runs are located at  $\sim 1 \text{ pc}$ , and move out with time. The radial positions of these shocks also increase with increasing spin parameter,  $\lambda$ , as the centrifugal barrier is reached at progressively larger radii. Figure 3 displays the shock locations as function of time, from their formation time to the end of the simulations. Note, that for a specific  $\lambda$ , both AMR and SPH shocks strictly follow each other. Moreover,

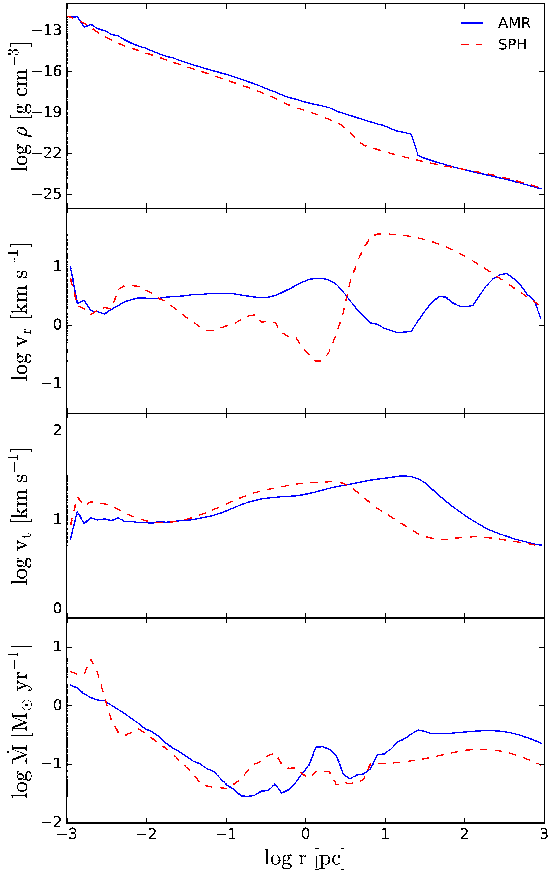


**Figure 2.** From top to bottom, radial profiles of gas density, radial velocity, tangential velocity, and mass accretion rate, at the end of the isolated runs for models AMR-I5 (solid lines) and SPH-I5 (dashed lines). All axes are logarithmic. The density and accretion rates have been averaged over spherical shells, and the velocities averaged over cylindrical shells.

consistently, the AMR shocks reach larger radii, as shown in Figure 3 for all  $\lambda$ . The explanation for this difference comes from the fact that the isolated AMR models collapse later than the isolated SPH models, as we discuss below, and shocks have more time to advance.

As a first step, we compare the radial profiles of a gas density, radial and tangential velocities, and accretion rates at the end of the runs, i.e., when the collapse has reached  $R_{\text{fin}}$  (Fig. 2). All values are given after averaging in cylindrical or spherical shells and at the run end. The gas density and accretion rates have been averaged over spherical shells, and the velocities averaged over cylindrical shells. Shown are the representative AMR-I5 and SPH-I5 runs. In AMR-I5 run, the gas goes through a strong accretion shock and forms a disk, ending the first stage of the collapse. By the end of the runs, the SPH-I5 shock is positioned at a radius about 3 times smaller than in the AMR-I5, which is confirmed by Figure 3. It appears also somewhat weaker than the AMR shock. In all other respects, the gas density profiles are very similar, albeit it takes another decade in radius for the density in SPH-I5 to catch up with the AMR-I5 density

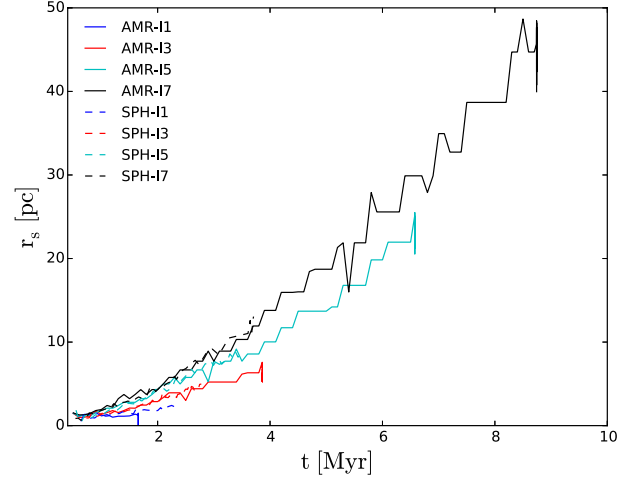


**Figure 3.** Evolution of the radial position of shocks,  $r_s$ , in isolated models in Enzo (solid lines) and GADGET-3 (dashed lines) runs for various  $\lambda$ . Note that both AMR and SPH runs with the same  $\lambda$  exhibit the same  $r_s(t)$ . The maximal  $r_s$  correspond to the end of the simulation.

just inside the shock. The final density is  $\rho \sim 10^{-14} \text{ g cm}^{-3}$  at  $R_{\text{fin}} = 10^{-3} \text{ pc}$ .

The radial velocity profiles,  $v_r$ , are very similar in the outer few hundred pc. In the preshock region, both  $v_r$  increase toward the center, then fall down substantially to a deep minimum in the post-shock region, at the respective positions of the shocks in the AMR and SPH runs. At smaller radii of  $r < 10^{-2} \text{ pc}$ , the curves are very similar and increase by an order of magnitude toward  $R_{\text{fin}}$ . The tangential velocities,  $v_t$ , reach maximal values in the post-shock region of both runs, as expected, then decrease toward the center. The behavior of  $v_r$  and  $v_t$  with  $r$  is associated with a variable degree of rotational support with radius, as we discuss below.

The mass accretion rate profiles show a similar behavior, but  $\dot{M}$  differs by a factor of 3 in the preshock region, where  $\dot{M} \sim 0.6 M_{\odot} \text{ yr}^{-1}$  for the AMR run and  $\sim 0.2 M_{\odot} \text{ yr}^{-1}$  for the SPH run. This rate drops to below  $\sim 0.1 M_{\odot} \text{ yr}^{-1}$  at  $R < 10 \text{ pc}$  for both runs. The 2nd stage of the collapse inside  $\sim 0.1 \text{ pc}$  displays a nearly identical behavior — both curves show a linear growth with decreasing  $r$ , reaching  $\dot{M} \sim 0.5 M_{\odot} \text{ yr}^{-1}$  at  $R_{\text{fin}}$ . The small spike in the SPH run at  $r \sim 10^{-3} \text{ pc}$  is caused by insufficient mass resolution there.

The projected gas volume density shown in Fig. 4 emphasizes both similarities and differences, in comparison with the 1-D radial density profiles. The most significant difference is that of the central disk size in the top frames — disk radius of  $\sim 20 \text{ pc}$  in the AMR-I5, and only  $\sim 7 \text{ pc}$  in the SPH-I5. This difference clearly has its origin in the position of the radial shock in both runs, as discussed above. So both disks appear shock-bounded. In the top frames, we also see a pronounced spiral structure in the AMR run, and a weaker one in the SPH run. The same conclusion can be reached from 5 pc scale images (middle and bottom panels), where  $m = 2$  (gaseous bar) is seen within the central 0.3 pc, and  $m = 3$  mode is driving a triple spiral on scales  $\gtrsim 0.5 \text{ pc}$ .

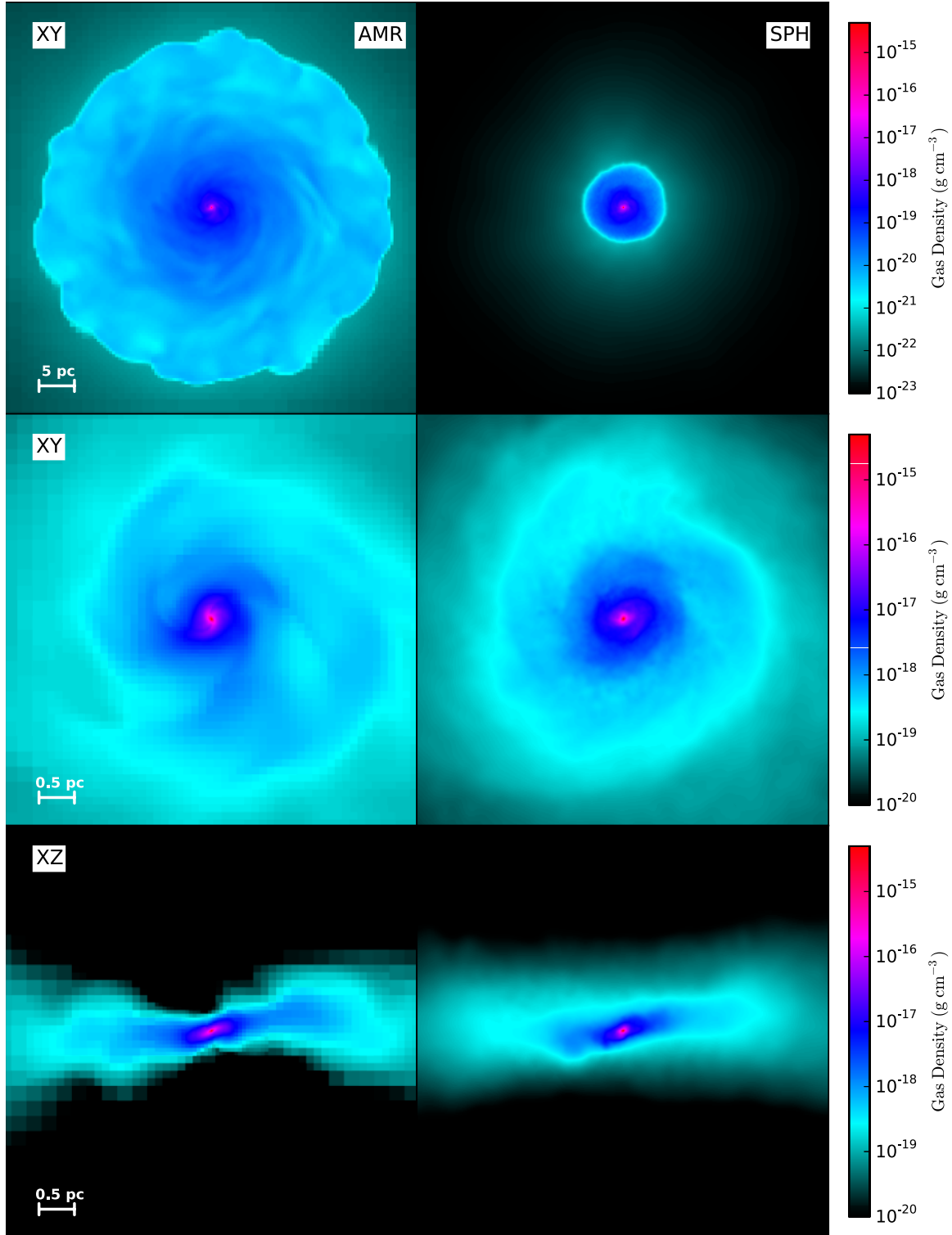


**Figure 4.** Mass-weighted gas volume density in the  $x$ - $y$  equatorial plane (top and middle frames) and the  $x$ - $z$  plane (bottom) of isolated models AMR-I5 (left frames) and SPH-I5 (right frames), at the end of the runs. Shown are the snapshots of decreasing spatial scales (physical): 50 pc (top) and 5 pc (middle and bottom) on each side, respectively. The color palette reflects the range from minimum to maximum densities in each panel. The face-on and edge-on disks can be seen clearly in both runs.

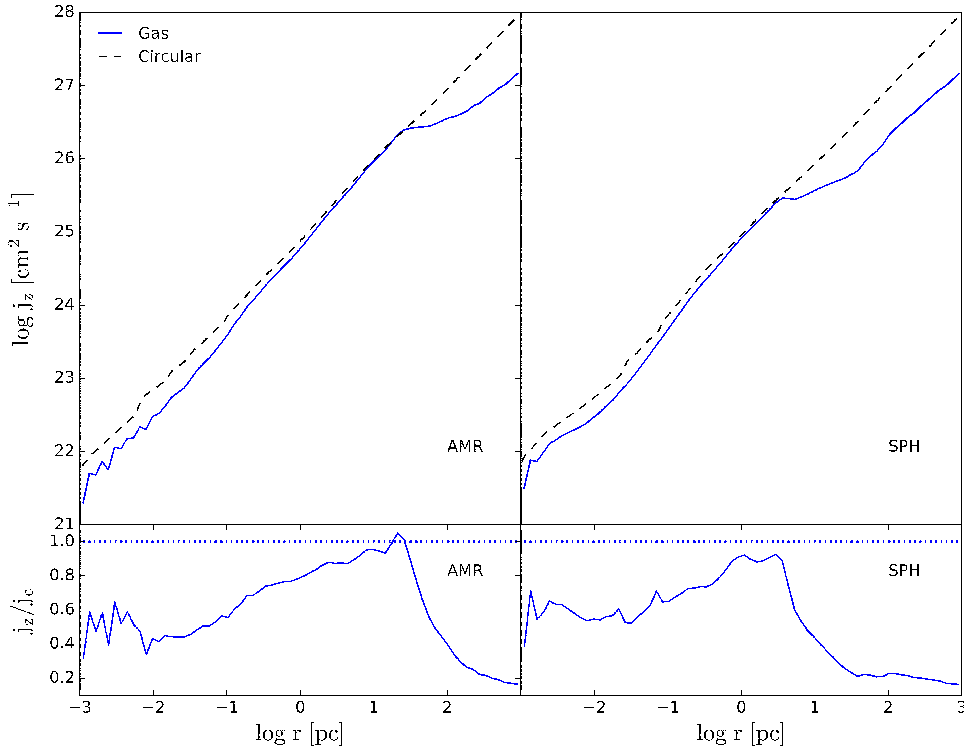


**Figure 5.** Specific angular momentum profile in the gas as a function of cylindrical radius for AMR-I5 (left panel) and SPH-I5 (right panel). Circular angular momentum profile is shown for comparison (dashed line).

The SPH-I5 run displays comparable  $m = 2$  and 3 modes on the same scales.

Redistribution of the angular momentum is an important ingredient of gravitational collapse. We compare specific angular momenta,  $j_z$ , in the gas at the end of the simulations, in AMR-I5 and SPH-I5 (Fig. 5). Two important differences can be observed. Positions of radial shocks (Fig. 2) corresponds to the radii where the specific angular momenta curves come close to the circular angular momenta,  $j_z \sim j_c$ . At smaller radii,  $j_z$  moves away from  $j_c$  gradually. Still, there is a non-negligible rotational support at  $R_{\text{fin}}$ , in both runs, albeit smaller for the SPH-I5 run. The bottom frames of this Figure provide the quantitative measure of rotational support in the form of  $j_z/j_c$  radial profiles. The AMR exhibits a disk at larger radii than the SPH run, because it takes more time for the AMR model to collapse, and, therefore, the accretion shock has more time to propagate outwards. In the 2nd stage of the collapse, i.e., inside  $\sim 1$  pc, the  $j_z/j_c$  ratio declines inwards, and showing a plateau for  $\lesssim 10^{-2}$  pc, at about 0.5. They demonstrate that, in the isolated models, rotational support for the collapsing gas never falls below  $\sim 50\%$  in the 2nd stage, in both runs.

The  $T - \rho_g$  relation is shown in Figure 6 at the end of the representative AMR-I5 and SPH-I5 runs. While the upper envelope of  $T$  is similar in both models, there appears to be much more gas at lower  $T$  at low densities,  $\rho < 10^{-20} \text{ g cm}^{-3}$ , in the AMR-I5 run. Given our refinement criteria, this is an anticipated property of mesh codes which are able to follow the low-density gas, while SPH codes tend

to resolve better the higher density regions. On the other hand, a larger amount of low  $T$  gas appears to be present at high densities,  $\sim 10^{-18} - 10^{-17} \text{ g cm}^{-3}$ , in the SPH-I5 run. We note that AMR run has larger mass accumulated (at  $\rho \sim 10^{-20} \text{ g cm}^{-3}$ ) around the shock, due to a larger shock radius, as evident from Figure 3. Since we use identical cooling packages for all runs, this difference can arise from the ability of numerical schemes to resolve the shocks and the cooling of a post-shock gas. In the AMR-I5, the radial shock is strong and advances to larger radii corresponding to lower gas densities of  $\sim 10^{-21} \text{ g cm}^{-3}$ . The low  $T$  gas is formed from the post-shock gas which cools down more efficiently. On the other hand, the SPH-I5 shock is weaker and happens at  $\sim 10^{-19} \text{ g cm}^{-3}$ , where particles at lower  $T$  already are much more common. Hence the shocked particles' contribution is hardly visible on the phase diagram.

Figure 7 compares various parameters which affect the resolution in AMR and SPH runs. The left panel shows evolution of maximal density in the gas,  $\rho_{\text{max}}$ , with time. Clearly, the collapse in the isolated model SPH-I5 proceeds much faster than in AMR-I5 already during the 1st stage. At the onset of 2nd stage, the density increases slowly, exhibiting kind of a plateau, then accelerates, and at the end of this stage  $\rho_{\text{max}}$  increases rapidly. Both runs display an identical behavior at the end.

The evolution of  $\rho_{\text{max}}$  allows us to quantify the separation of the two stages of the collapse (see also Choi et al. 2013). The plateau between the stages provides an independent quantitative support to the existence of these stages.



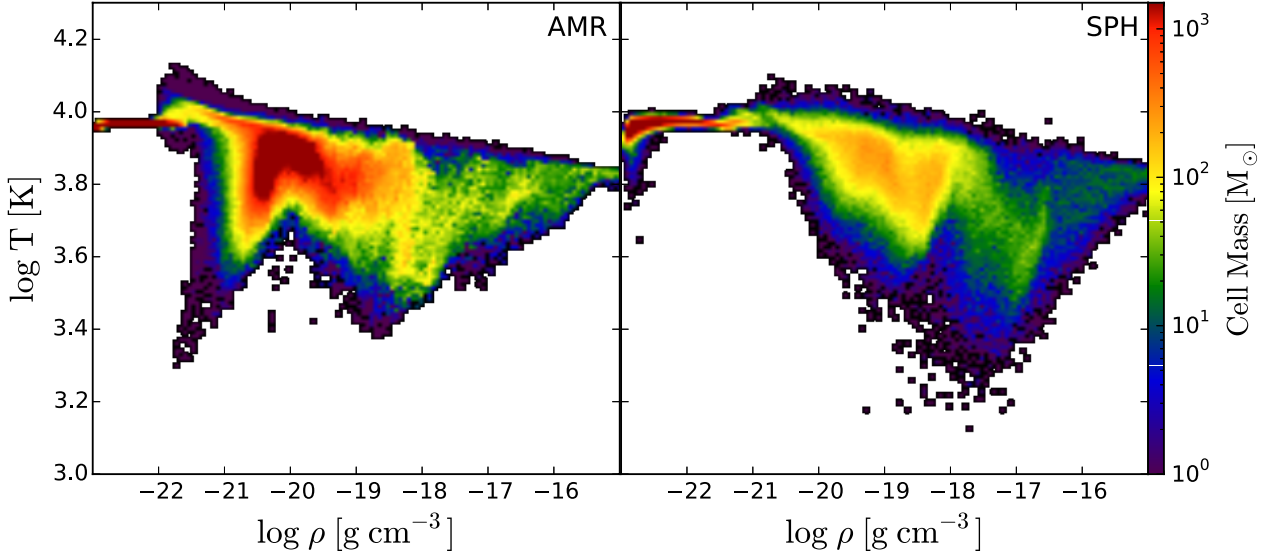


**Figure 6.** Phase diagram of temperature vs. density of gas in isolated runs AMR-I5 (left panel) and SPH-I5 (right panel) at the end of each run. The color represents the amount of mass in each pixel.

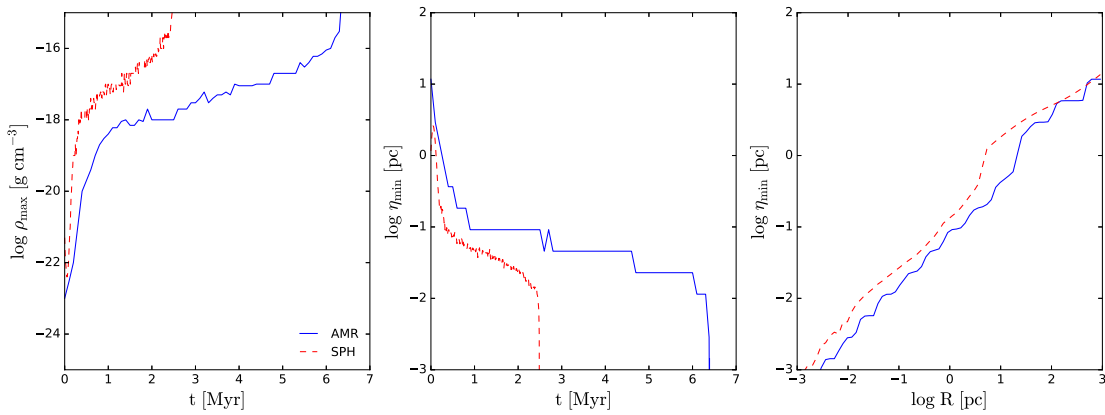


**Figure 7.** Comparing various resolution parameters for isolated models AMR-I5 (solid lines) and SPH-I5 (dashed lines). *Left panel:* Evolution of maximum gas density  $\rho_{\max}$  as a function of time. *Middle panel:* Evolution of the minimal gas smoothing length for the SPH and minimum cell size for the AMR run,  $\eta_{\min}$ , as functions of time. *Right panel:* Radial profile of resolution given by the smoothing length for SPH and the minimum cell size at each radius for AMR, at the end of the runs. The 1st stage of the collapse which starts at  $t = 0$  is identical for both models. The 2nd stage of the collapse is triggered when the gas-to-DM density ratio in the inner few pc exceeds unity, i.e.,  $\sim 2.4$  Myrs for GADGET and  $\sim 6.3$  Myr for Enzo. Note, that after the onset of the 2nd stage of the collapse, the collapse proceeds on a very short timescale as observed by the sharp drop in  $\eta_{\min}$  (middle panel).

They are also observed in the evolution of the minimum gas smoothing length for SPH and minimum cell size for AMR,  $\eta_{\min}$ , shown in the middle frame of Figure 7 — this frame describes the same process of  $\rho_{\max}$  but in terms of the gas minimal smoothing length  $\eta_{\min}$ , which is the minimal interparticle distance Following Choi et al. (2013, 2015)

and Shlosman et al. (2016), we choose to define the beginning of the 2nd stage when the gas-to-DM density ratio becomes larger than unity within the central few pc. This happens at  $t \sim 2.4$  Myr in SPH-I5 and  $\sim 6.3$  Myr in AMR-I5. The collapsing gas reaches the final resolution of

**Table 3.** DM halo virial parameters in AMR and SPH cosmological models at the time of direct collapse, i.e., at  $z_{\text{coll}}$ .

| Models   | $z_{\text{coll}}$ | $M_{\text{vir}} [h^{-1} M_{\odot}]$ | $R_{\text{vir}} [h^{-1} \text{pc}]$ |
|----------|-------------------|-------------------------------------|-------------------------------------|
| AMR-C1.5 | 17.2              | $2.4 \times 10^7$                   | 407                                 |
| AMR-C2.8 | 11.9              | $4.7 \times 10^7$                   | 722                                 |
| AMR-C4.2 | 19.3              | $2.7 \times 10^7$                   | 379                                 |
| SPH-C1.5 | 15.5              | $4.1 \times 10^7$                   | 538                                 |
| SPH-C2.8 | 11.0              | $5.4 \times 10^7$                   | 809                                 |
| SPH-C4.2 | 18.6              | $3.4 \times 10^7$                   | 422                                 |

$\eta_{\text{min}} \sim \text{few} \times 10^{-3}$  pc at  $\sim 2.4$  Myr and  $\sim 6.3$  Myr, respectively. At this time the collapse has reached  $r_{\text{fin}}$ .

The final radial profile of  $\eta_{\text{min}}$  is shown in the right panel of Figure 7. Both AMR and SPH curves for  $\eta_{\text{min}}$  are similar, but still the AMR one is systematically lower by a factor of 2 – 3 depending on the radius.

### 3.2 Direct collapse in cosmological models

For cosmological models, we stop the runs when the AMR and SPH resolutions, measured by  $\eta_{\text{min}}$ , reach  $R_{\text{fin}} \sim 10^{-2}$  pc. The reason for this is that high resolution of isolated models is more difficult to reach in cosmological runs. Therefore, we reduce the resolution demands in both AMR and SPH cosmological models by a factor of 10 compared to the isolated ones. The time is measured from the Big Bang.

As the DM halos form and grow with time in the cosmological models, the DM density profiles tend to the NFW shape (Navarro et al. 1997). When the collapse reaches the central regions, the baryon drag in the DM and form a cusp, similar to that in isolated models. Note, that our isolated models follow the isothermal sphere density profiles and not the NFW ones. We shall return to this issue in § 4.

We show the gas density, radial and tangential velocity, and mass accretion rate profiles for a representative cosmological models AMR-C4.2 and SPH-C4.2 with  $\lambda \sim 0.042$  — very similar to the representative isolated cases (Fig. 8). We have also measured the DM halo virial masses and virial radii for Enzo and GADGET cosmological models at the time of direct collapse,  $z_{\text{coll}}$  (Table 3). Overall, the AMR models collapse slightly earlier than the SPH ones. Consequently, the DM halos appear slightly less massive and their virial radii slightly smaller. So a pronounced trend exists between the AMR and SPH cosmological models.

The top panel displays the final density profiles which are remarkably similar for the two runs. While density at  $R_{\text{fin}} \sim 10^{-2}$  pc is nearly identical to that in the corresponding isolated runs, the overall shape of  $\rho(R)$  somewhat differs. In the isolated runs, inside the radial shock, the slope of  $\rho(R)$  was nearly constant, while in the cosmological runs it exhibits the trend of becoming shallower with  $R$ . This change happens at  $R \sim 0.5 - 5$  pc, continues inward, and appears slightly more pronounced in AMR than in the SPH runs. It appears to be the result of our use of an isothermal density profile for the DM in isolated models, and the formation of less cuspy NFW DM profiles in the cosmological runs. Another major difference between isolated and cosmological models is the absence of standing radial shock, which we explain below.

The radial velocities in AMR-C4.2 and SPH-C4.2 vary

within a factor of a few along  $r$ , but end up similar within a factor of 2 at the center. The tangential velocity is consistently higher in AMR at  $r \gtrsim 0.2$  pc, then reverse the trend with the AMR velocity becomes smaller than SPH one at  $r \lesssim 0.2$  pc.

The bottom panel of Figure 8 displays the radial profile of mass accretion rate,  $\dot{M}$ . The curves differ by a factor  $\sim 2 - 3$  among themselves, in the outer radii, and  $\lesssim 2$  inside 50 pc. But they also differ profoundly from their isolated counterparts. First they exhibit a deep minimum at  $r \sim 50 - 100$  pc and stay about constant,  $\dot{M} \sim 1 - 3 M_{\odot} \text{yr}^{-1}$  inward. The reason for this behavior is increased rotational support they experience in this region, i.e.,  $v_r$  and  $v_t$  have local minima and maxima there. On the other hand, the isolated models display growing  $\dot{M}$  toward  $r_{\text{fin}}$  and reach a maximum there which is greater than the cosmological case by a factor of 2. The cosmological  $\dot{M}$  is higher by a factor of a few everywhere except at the very center. Lastly, at the center, for  $R \lesssim 0.1$  pc, the mass accretion in the SPH run falls by almost an order of magnitude, and less so in the AMR run.

Figure 9 compares the projection snapshots for DM and volume densities for the gas of representative cosmological simulations from identical initial conditions for Enzo (left panels) and GADGET-3 (right panels). The extracted DM halos have  $\lambda = 0.042$ . The snapshots have been taken at the end of the runs, when the collapse have reached  $R_{\text{fin}} \sim 0.01$  pc. The top panels show the large scale distribution of the DM on scales of  $100 h^{-1}$  kpc (comoving). Some differences are noticeable in these frames, and typically can be attributed to individual DM halos. Indeed, we focus on the representative DM halos in the second row within (approximately) their virial radii, with the box size of  $5 h^{-1}$  kpc (comoving). Again, while overall a nice degree of similarity exists between the two runs, differences are clear as well, especially if one focuses on the substructure on this scale. The bottom panels show the corresponding gas distribution within these halos, on scales of  $200 h^{-1}$  pc (comoving). While the AMR panel displays the characteristic filamentary structure, the SPH panel shows a rather centrally-concentrated, elongated gas distribution, although the central density is the same in both runs. The SPH density distribution displays less small-scale structure in general. The AGORA collaboration (Kim et al. 2014) has also reported difference in substructure within the similar large-scale structure.

Next, we show the radial distribution of the specific angular momentum profile at the end of the simulations, as well as  $j_z/j_c$  ratio (Fig. 10). Clearly, both runs display much less angular momentum support at all radii compared to the isolated models. On top of this, the SPH run shows even less support than the AMR one, and proceeds basically in the free-fall fashion until it has reached  $r \sim 0.1$  pc. The explanation for such a dramatic difference between the rotational support in isolated and cosmological models is related to the efficiency of angular momentum extraction from the gas by the background DM. In the former models, the DM halos are nearly axisymmetric, while in the latter case, they are substantially triaxial. Resulting gravitational torques from the DM onto the gas will be largely suppressed in the isolated models, and the gas will have stronger rotational support.

We also show the comparison between the  $T - \rho$  maps for the above models in Figure 11. The overall feature of

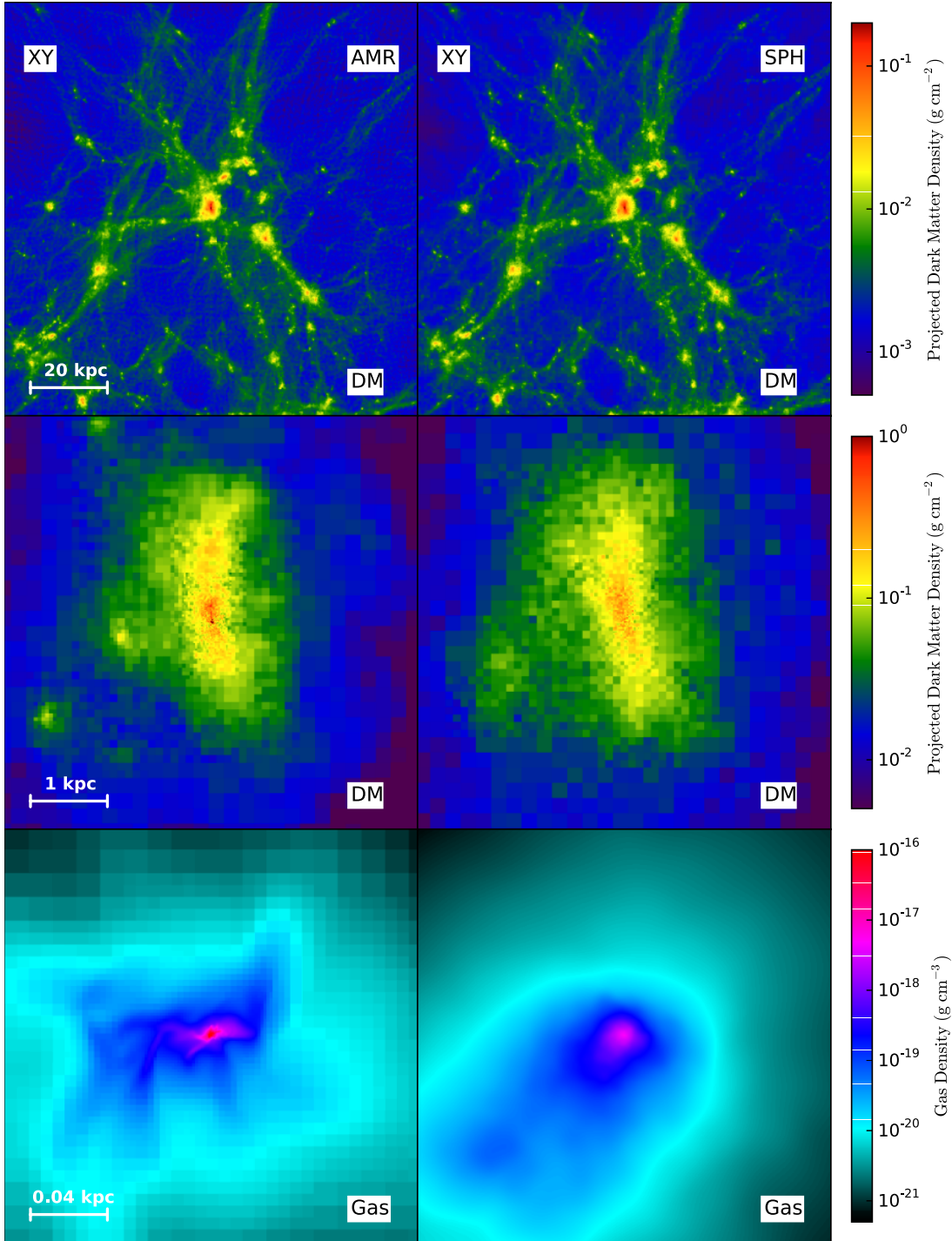


**Figure 9.** Projections of final DM density in  $x-y$  plane in cosmological models AMR-C4.2 (left column) and SPH-C4.2 (right column). The spatial scale of each panel decreases from top to bottom: DM in 100 kpc (comoving), DM in 5 kpc (comoving), and mass-weighted gas volume density in 200 pc (comoving), respectively. The depth of each frame is 10 kpc (top), and 0.5 kpc (middle) in comoving coordinates. The color palette reflects from minimum to maximum projection densities in each panel.

the phase diagrams are very similar between the two runs, with the exception of the mass involved at particular  $T$  and  $\rho$  values. At high densities, the AMR run shows a somewhat broader distribution in  $T$ -range with very small mass contained in each grid-cell, which are completely absent in the SPH run. This is understandable, as the two codes have a different resolution at these densities. Although we start

from identical initial conditions in Enzo and GADGET-3, the refinement history differs between the codes in detail. We have tested how sensitive is the evolution with respect to the refinement condition in Enzo and discuss it below.

To specify the characteristic times of gravitational collapse in the cosmological models, we follow the definition from isolated models. The onset of the 1st stage of the col-

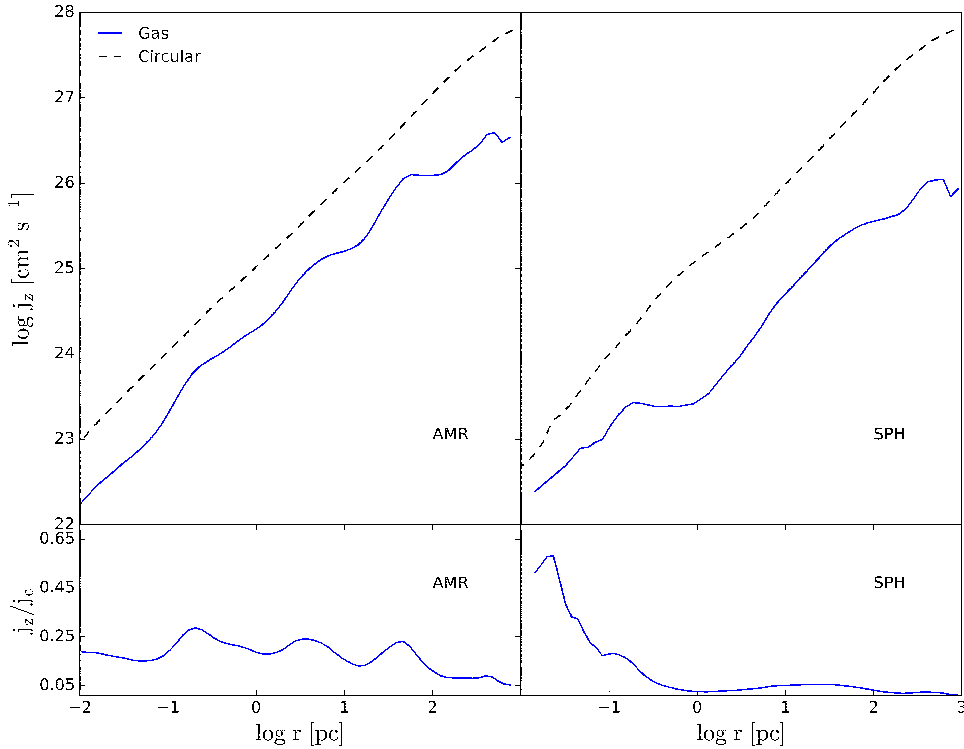


**Figure 10.** Specific angular momentum profile of gas as function of cylindrical radius for Enzo (left panel) and GADGET3 (right panel) in the cosmological runs AMR-C4.2 and SPH-C4.2. Circular angular momentum profile is shown for comparison (dashed line).

lapse is inferred from the sudden rise in refinement level in Enzo and from  $\eta_{\min}(t)$  in GADGET. The 2nd stage is triggered when the gas-to-DM density ratio exceeds unity in both Enzo and GADGET.

The left panel of Figure 12 shows the time evolution of  $\rho_{\max}$  in cosmological simulations. The time prior to  $t \sim 178$  Myr corresponds to DM structure formation. It involves the initial expansion and collapse of DM shells, forming a small DM halo, which we target in the zoom-in simulations. This halo grows via accretion of cold gas and DM — a process permeated by merger events. As the halo approaches the critical mass of  $\sim 10^8 M_{\odot}$ , direct baryonic collapse follows. The gas collapse starts around 178 Myr and proceeds rapidly (but slower than in the isolated models), being triggered nearly simultaneously in both runs.

The middle frame of Figure 12 displays the evolution of the minimal smoothing length,  $\eta_{\min}$ , in the gas. Again, until the onset of the gravitational collapse, the AMR curve displays a better resolution compared to the SPH one, by a factor of 2–3, but both codes are resolving basically the same densities at this time (see § 4 for more details). This difference appears during the initial collapse and formation of the targeted DM halo. With the onset of direct collapse at  $t \sim 178$  Myr, this difference in  $\eta_{\min}$  gets amplified and the collapse proceeds increasingly faster in the AMR run. This is a reverse situation with respect to isolated models, and shows up explicitly in the radial profiles of  $\eta_{\min}$ . We expect that the run with a smaller  $\eta_{\min}$  will collapse first. We note that the duration of the baryonic collapse here,

$\sim 10 - 20$  Myr, is substantially longer than in respective isolated models. The reason for this difference comes from the collapse inside NFW halos which have a substantially lower central DM densities than in similar isothermal spheres used by us for isolated models.

The right frame of Figure 12 displays the radial profile of  $\eta_{\min}(R)$  at the end of cosmological simulations AMR-C4.2 and SPH-C4.2. Note, the bifurcation in  $\eta_{\min}$  at around few pc from the center of the DM halo. Whereas the outer halo region is equally resolved with both runs, the inner one is better resolved with the AMR. This explains why the 2nd stage of the collapse proceeds faster with Enzo.

### 3.3 Effect of host DM halo spin on isolated models

As additional and a broad test for model comparison, we measure the collapse time in each model and contrast the Enzo-2.4 and GADGET-3 runs in isolated models. Effect of gas rotation on gravitational collapse has been also modeled by Jappsen et al. (2009) in the context of Pop III star formation. However, they assumed a *rigid* spherical DM halo which, therefore, cannot absorb angular momentum and/or produce gravitational torques on the gas.

To analyze the collapse time for isolated models, we measure the time from the start of the run, using models with a range in the spin parameter  $\lambda$ , for AMR and SPH runs. In other words, we define the collapse time,  $\Delta t_c$ , as

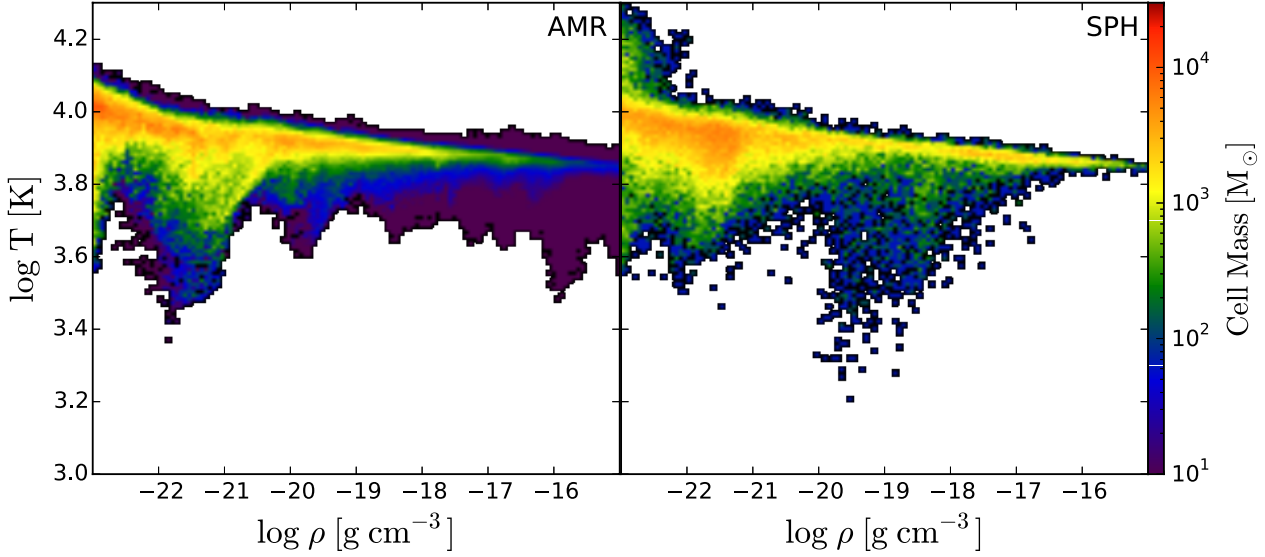


**Figure 11.** Phase diagram of temperature vs. density in AMR-C4.2 (left panel) and SPH-C4.2 (right panel) at the end of the cosmological model simulations. The color represents the mass in each pixels.

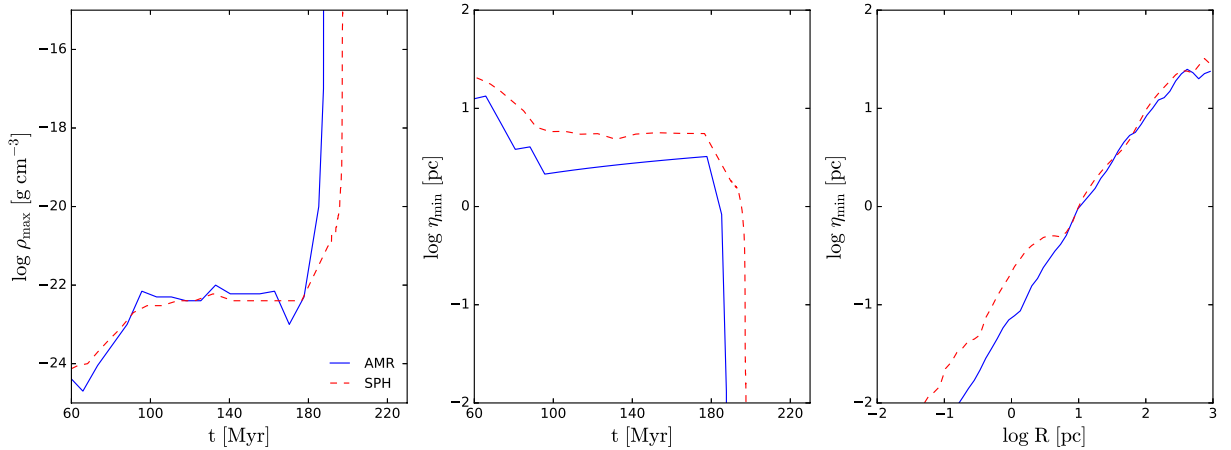


**Figure 12.** Same as Figure 7, but for cosmological models AMR-C4.2 (solid lines) and SPH-C4.2 (dashed lines). Note, that the collapse starts around  $t \sim 178$  Myr for AMR and SPH runs, when  $\rho_{\max}$  and  $\eta_{\min}$  are slightly in favor of the AMR, compared to being identical in the isolated models.  $\eta_{\min}(R)$  shows that the innermost resolution is higher in Enzo inside few central pc, while it is identical in the outer DM halo.

the time from  $t = 0$  till the collapse reaches  $R_{\text{fin}} = 10^{-3}$  pc (§ 2.2). The collapse time,  $\Delta t_c$ , is given in Figure 13.

For isolated models, two trends can be observed. First, both AMR and SPH runs exhibit a monotonic increase of  $\Delta t_c$  with  $\lambda$ , up to the measured spin of  $\lambda \sim 0.07$  (Fig. 13). Second, the AMR runs display a longer collapse time than the SPH runs. As a corollary, the difference between the

collapse time of AMR and SPH runs is increasing monotonically with  $\lambda$ .

The first trend can be easily explained. With increasing DM halo spin parameter, the gas must overcome a centrifugal barrier positioned at progressively larger radii, because the initial conditions for the isolated runs require the gas to have the same specific angular momentum  $j(r)$  distribution

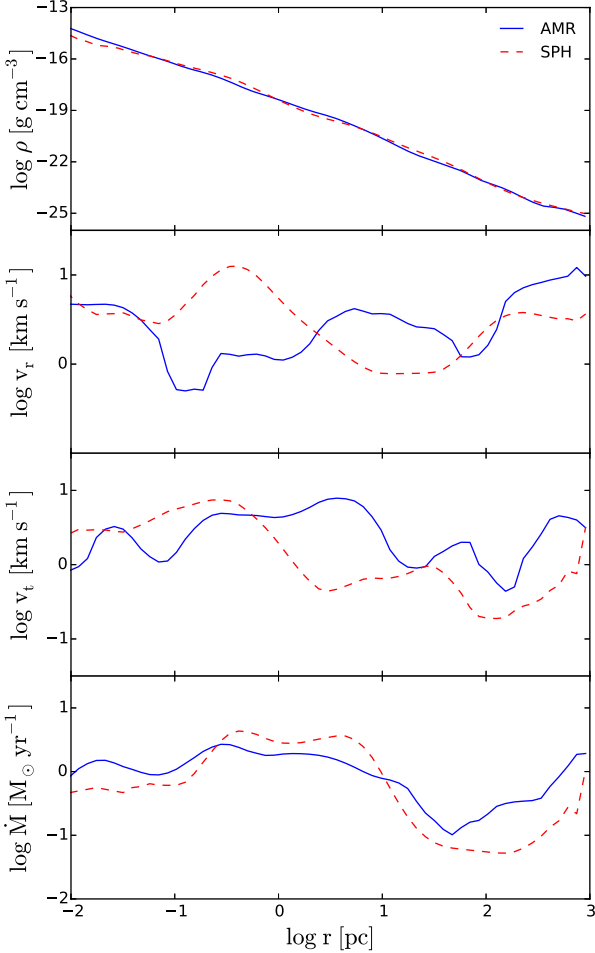


**Figure 8.** From top to bottom, radial profiles of gas density, radial velocity, tangential velocity, and mass accretion rate, at the end of the cosmological runs for models AMR-C4.2 (solid lines) and SPH-C4.2 (dashed lines). All axes are logarithmic. The density and accretion rate have been averaged over spherical shells, and velocities averaged over cylindrical shells.

as the DM. The gas evolution is complicated by the intricacies of gravitational collapse: gas at small radii collapses first and it has lower  $j$  than the gas at larger radii. So the initial circularization determines the position of the accretion shock which forms at  $\sim 1$  pc from the center, as seen in Figure 3. As the gas with larger  $j$  circularizes at larger  $r$  progressively later, the shock moves out, and does it faster for larger  $\lambda$ . Hence, the size of the forming disk behind the accretion shock is increasing with  $\lambda$  and with time (e.g., Fig. 3).

For the second stage of the collapse to ensue, the gas must decouple from the background DM potential, i.e., its density must increase above the DM density at small radii (e.g., § 3.1 of Choi et al. 2013, 2015). In isolated models this is approximately the radius of the disk which forms behind the standing accretion shock. Naturally, a larger accumu-

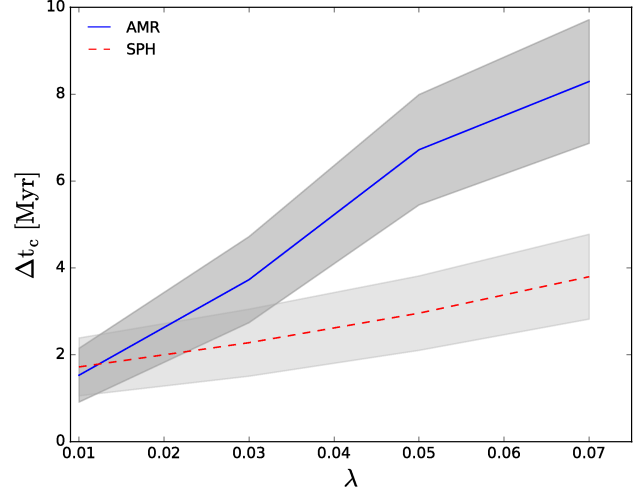


**Figure 13.** Duration of gravitational collapse time for isolated models,  $\Delta t_c$ , in Enzo-2.4 and GADGET-3 runs as function of the halo spin parameter  $\lambda$ . The grey region represents  $\pm 1\sigma$  errors using the Poisson statistics.

lation of baryons is required when decoupling happens at larger radii, explaining the increased  $\Delta t_c$  for larger  $\lambda$ . Indeed, the disk sizes and, therefore, masses increase with  $\lambda$ .

Hence, this simple physics explains the relatively modest increase in  $\Delta t_c$  with  $\lambda$ . Remarkably, both Enzo and GADGET-3 runs agree in their  $\Delta t_c$  for  $\lambda = 0.01$ . But what about the increasing delay in the collapse time of the AMR runs with  $\lambda$ ? To understand this, one should look carefully into different resolution pattern of both codes. While initial conditions are identical in this respect, the SPH gravitational softening is constant with time, while that of the AMR code are refined as the collapse proceeds. This by itself does not have a direct effect on the dynamics, but there are caveats. Probably the most important issue is the possible effect that refinement has on the development on degree of turbulence in the collapsing gas.

In Figure 14a, we show evolution of  $\eta_{\min}$  for three representative  $\lambda$  for Enzo and GADGET-3. For  $\lambda = 0.01$ ,  $\eta_{\min}(t)$  displays little difference between Enzo-2.4 and GADGET-3. For higher spin, we observe an increasing delay in the 2nd stage of the collapse, especially for Enzo runs. Checking the associated increase in the refinement levels, the latter appears to stagnate before the onset of the 2nd stage of the collapse. In other words,  $\eta_{\min}$ , which reflects the best spatial resolution at each time, as mentioned above, “hesitates” to decrease for a longer time in Enzo compared to GADGET-3. Therefore, we observe a longer plateau for Enzo in Figure 14.

### 3.4 Effect of host DM halo spin on cosmological models

In the previous section, we have measured the collapse timescales for isolated models and contrasted them between Enzo-2.4 and GADGET-3 runs. Similar exercise in cosmological models is more complicated, because it involves cosmological evolution of DM halos, which depends on struc-



ture formation in the universe and results in halos having different shapes and other properties. Hence, while a detailed comparison of the collapse time for cosmological models is outside the scope of this work, we do compare some numerical aspects of their evolution with various  $\lambda$ .

We define the cosmological collapse timescale,  $\Delta t_c$  by following the evolution of the baryonic refinement level, the maximal hydrodynamic resolution,  $\eta_{\min}$ , and the maximal density,  $\rho_{\max}$  — all defined as in isolated models. The beginning of the direct collapse in the cosmological DM halos,  $t_0$ , is determined when these parameters exhibit a sharp increase or decrease, correspondingly. For example,  $\eta_{\min}$  decreases sharply at  $t \sim 178$  Myr, which is considered as the onset of the collapse. The end point of the collapse is taken  $t_{\text{fin}}$ , when it reaches  $R_{\text{fin}}$ , and  $\Delta t_c = t_{\text{fin}} - t_0$ . To detect a sharp increase/decrease in  $\rho_{\max}$  and  $\eta_{\min}$ , we follow their time derivatives after  $\sim 140$  Myr and test all the occurrences for the increase/decrease by a factor of 2 or more.

We repeat the  $\lambda$ -test discussed in the previous section, for cosmological models. Naively, one expects to observe the same correlation between  $\Delta t_c$  and  $\lambda$  shown in Table 4 and in Figure 13. However, as exhibited by Figure 14b, this is not the case. For three representative cosmological models in AMR and SPH, the one-to-one correlation between  $\Delta t_c$  and  $\lambda$  does not exist here. Why does this happen?

A number of physical reasons in cosmological models would ‘mess up’ this correlation. First, the host DM halos in isolated models are axisymmetric. This means that collapsing gas has difficulty to lose angular momentum to DM, and loses it mostly to gas. On the other hand, the DM halo shapes in cosmological models differ profoundly from axisymmetric shapes. Therefore, the gas will lose its angular momentum continuously and efficiently to the DM, which will move the gas away from the centrifugal barrier at each radius, as in fact is shown in Figure 10.

Secondly, because the direct collapse takes about 10 – 20 Myrs in cosmological models, the basic properties of DM halos can change during this time. They can undergo minor, intermediate and major mergers. In other words, the host halos will have enough time to interact with the substructure — which does not happen in isolated models.

These and additional factors are expected to affect the direct collapse onset and duration in cosmological simulations in a kind of unpredictable way, which we indeed observe in our simulations.

For isolated and cosmological SPH and AMR models, the free-fall time for the DM halos at the onset of direct collapse is  $t_{\text{ff}} \sim 35$  Myr. In comparison with the actual collapse timescales given in Table 4, the collapse times are shorter than the free-fall times. This underlines an important point that direct collapse involves only the inner part of the gas initially residing in DM halos.

## 4 DISCUSSION & CONCLUSIONS

We have performed comparison simulations of gas collapse in DM halos in the context of direct collapse scenario to form SMBH seeds using AMR and SPH codes. This problem involves large dynamic range, from kpc down to AU scales — such a comparison has not been attempted before. Using Enzo-2.4 AMR and GADGET-3 SPH codes, we ex-

**Table 4.** Values of  $\Delta t_c$  for isolated and cosmological models shown in Figure 14. The definitions of  $\Delta t_c$  are given in §§ 3.3 and 3.4 for isolated and cosmological models, respectively.

| Models   | $\Delta t_c$ (Myr) |
|----------|--------------------|
| AMR-I1   | 1.7                |
| AMR-I5   | 6.3                |
| AMR-I7   | 8.3                |
| SPH-I1   | 1.7                |
| SPH-I5   | 2.3                |
| SPH-I7   | 3.4                |
| AMR-C1.5 | 14.6               |
| AMR-C2.8 | 17.5               |
| AMR-C4.2 | 14.3               |
| SPH-C1.5 | 20.6               |
| SPH-C2.8 | 19.8               |
| SPH-C4.2 | 20.6               |

amined the systematic differences which buildup when these numerical schemes are invoked. We made significant efforts to match the initial setup of the two simulations. We addressed the associated problems using isolated and cosmological models of gravitational collapse in DM halos with a range of cosmological spin parameter  $\lambda$ . To simplify this task, we ignored the effect of molecular hydrogen and UV background radiation, and assumed an optically-thin atomic cooling, as described in §§ 1 and 2. As a result, the collapse is nearly isothermal in all runs. Our main results are as follows:

- The isolated models generally follow similar evolutionary path and agree with Choi et al. (2013), but exhibit many subtle differences among themselves. Specifically, the collapse proceeds in two stages, first reaching the angular momentum barrier, going through an accretion shock, and forming a disk behind it. In the second stage, which begins after the gas density in the disk region surpasses that of the DM density, the gas decouples from the background gravitational potential of the DM and experiences a runaway collapse, dragging some of the DM inward in an adiabatic compression. We find that, although the AMR and SPH models start with identical initial conditions, the pace of increase in spatial resolution differs in both codes. This leads to a substantially earlier collapse in the SPH models for the isolated models.
- Cosmological models do not exhibit ‘standing’ accretion shocks, unlike their isolated model counterparts, and, consequently, do not form rotationally-supported disks. The reason for this is the continuous loss of angular momentum by the collapsing gas to the background triaxial potential of the host DM halos, contrary to isolated models which stay largely axisymmetric. Nevertheless, one can distinguish between first and second stages of the collapse, when the gas-to-DM density ratio crosses unity, within the central few pc. The cosmological evolution of DM halos and baryons appears to be similar among the AMR and SPH runs, being only slightly in favor of the AMR models in baryonic spatial and mass resolutions. But a pronounced trend exists between the AMR and SPH cosmological models, with the former exhibiting direct collapse at higher redshifts, and, consequently, the collapse happens in less massive and smaller DM halos. With the onset of baryonic gravitational collapse within DM halos, the pace of the resolution change differs

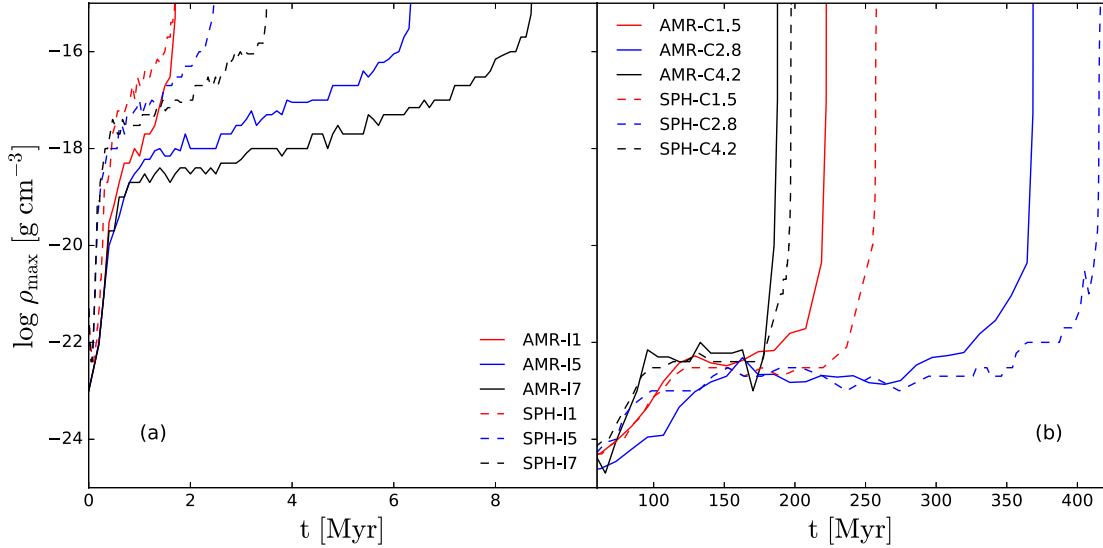


**Figure 14.** Comparison of the evolution of  $\rho_{\max}(t)$  for (a) three isolated models with  $\lambda = 0.01, 0.05$  and  $0.07$  for AMR-I1, -I5 and -I7 (solid lines) and SPH-I1, -I5 and -I7 (dashed lines) runs. (b) Same for three cosmological models, AMR-C1.5, -C2.7 and -C4.2 (solid lines) and SPH-C1.5, -C2.7, and -C4.2 (dashed lines). The collapse timescales,  $\Delta t_c$ , for these models are listed in Table 4.

among the codes and the resolution increases faster in the AMR runs. Consequently, the trend in the time-lag is reversed here with respect to the isolated models, and the AMR models collapse before the SPH models. Thus, a small difference in the pre-collapse resolution is amplified substantially during the collapse.

- The collapse time  $\Delta t_c$  increases with increasing  $\lambda$  in isolated models. Greater centrifugal forces divert the infalling gas to larger radii, i.e., circularization happens further away from the rotation axis. This is translated to larger expansion velocities of the accretion shocks and larger accretion disk sizes. Shock in the AMR runs propagate further out than in the SPH runs, because the final collapse time is later for the AMR isolated models.

- For cosmological models, the baryonic collapse time is much longer than in isolated models, because the average density in the central regions of the NFW halos is lower than that of the isothermal spheres by a factor of  $\sim 100$ , which leads to longer collapse time by a factor of  $\sim 10$ . Additional factors discussed above affect  $\Delta t_c$ , unlike in isolated models.

In this work we have focused on numerical aspects of gravitational collapse to the SMBH seeds, and so avoid discussing the associated physics, except when unavoidable. The main reasons for dissimilar performance of the AMR and SPH codes lies in the mismatch between the pace of increase in spatial and mass resolutions when comparing performance of the AMR and SPH codes. These differences appear to be profound and not easily reconcilable.

Both numerical codes under comparison here, AMR Enzo-2.4 and SPH GADGET-3, follow collisionless cold DM and dissipative fluid component. Each of these components is important in order to understand evolution of gravitational collapse. The DM plays a crucial role in diluting the gravitational interactions within the gas, and, therefore, increasing its Jeans mass. Together with development of virial

supersonic turbulence in the gas, it reduces the fragmentation in the collapsing flow, and allows the collapse to proceed via large dynamic range.

Most important is the resolution of the gravitational force. Enzo uses a multi-grid PM method, and therefore, its resolution is governed by twice the minimum cell size (§ 2.2). On the other hand, GADGET-3 uses the tree method to compute gravity, and its gravitational resolution is set by a fixed softening length. Hence, the forces are computed more accurately in GADGET-3 compared to Enzo, particularly at the initial stage of collapse, when Enzo has not refined many levels yet. In principle, one should be able to make the Enzo gravity resolution comparable to that of GADGET from the very beginning, by investing significantly larger number of initial mesh allocations, e.g., by nested initial grid. However, this was not feasible with reasonable computational resources for the present work.

In isolated models, we have been able to push the initial spatial resolution of Enzo to  $\sim 10$  pc with three initial nested grid levels. At the same time, GADGET has had a constant softening length of  $\epsilon_g = 10^{-4}$  pc for the SPH particles and  $\epsilon_{DM} = 0.37$  pc for the DM, from the beginning (see Table 2). Of course the particles are not as close as these distances from the start of the run, but the forces are computed accurately with the tree method down to  $\epsilon_g$  and  $\epsilon_{DM}$ . On the other hand, Enzo gravity was allowed to refine, but it did not refine fast enough to catch up with GADGET in the isolated models, judging from the evolution of the hydrodynamical resolution parameter,  $\eta_{\min}$ . For periods of time, Enzo refinement level has been constant, then changed abruptly. Thus, Enzo resolution always lagged behind GADGET in the isolated models. Due to these differences, Enzo was unable to follow the steep density cusp of the DM isothermal sphere in the center.

The above situation is similar to the one found in the context of cosmological simulation by O’Shea et al. (2005),



where Enzo and GADGET codes have been compared for cosmological structure formation. In this case, Enzo had to invest in  $\sim 256^3$  root-grid in order to reproduce the same DM halo mass function as the GADGET run with  $128^3$  particles. When simply using the root-grid of  $128^3$ , Enzo was unable to follow the growth of early density perturbations due to poorer force resolution, and it resulted in an underestimate of halo substructures and low-mass halos at early times. This means that Enzo AMR code requires significantly larger computing resources than GADGET SPH code in order to obtain similar structures on small scales, particularly in the context of cosmological structure formation.

In the present work, the context and the spatial scale of the problem is very different from that of O’Shea et al. (2005). Enzo’s main advantage is the refinement method which allows it to obtain a superior hydrodynamic or gravitational force resolution, albeit toward the end of the cosmological simulation and in a very small volume. Therefore, during the pre-collapse phase, when high resolution is not required, the difference in computational resources used by both codes are comparable, within a factor of two, in the CPU time. On the other hand, during the direct collapse in isolated and cosmological models, GADGET requires 5 – 10 times more CPU time than Enzo. Compared to Enzo, GADGET over-resolves in the initial stage of the collapse, and under-resolves in the final stages, unless SPH particle splitting method is used or the SPH has a dynamic gravitational softening, as in GIZMO (e.g., Heller & Shlosman 1994; Hopkins 2013).

The bottom line is that in our simulations of direct baryonic collapse in isolated and cosmological framework, GADGET requires greater investment in computational resources, but benefits from better hydrodynamic and gravitational force resolution in the computational box, while Enzo achieves a superior resolution in a very small volume.

Note that our cosmological models of direct collapse evolve similarly in the AMR and SPH cases. The left and middle panels of Figure 12 show that direct collapse happens nearly simultaneously in AMR and SPH runs, as exhibited by the behavior of  $\rho_{\max}$  and  $\eta_{\min}$ . But these two parameters differ by a factor of a few until the onset of the direct collapse at  $t \sim 178$  Myr. As the collapse develops, we observe that SPH lags behind AMR, unlike in isolated models, where the SPH models collapse first. The reason for this behavior can be observed in the right panel of Figure 12. Here the AMR has higher mass and spatial resolution than SPH in the inner few pc at the final phase of the collapse.

The delay in the collapse time can have a significant impact on the cosmological evolution of direct collapse, in the presence of an external UV background. The latter can dissociate  $H_2$  molecules, which is considered to be a critical factor for the success of this scenario (e.g., Omukai 2001; Latif et al. 2011; Inayoshi et al. 2014; Sugimura et al. 2014). If the collapse is delayed significantly, it might appear favorably for the direct collapse scenario because of the higher UVB intensity from nearby star formation, which should be increasing with time at redshifts  $z \sim 20$  to 10. In our current simulations, Enzo-2.4 and GADGET-3 give mixed results on the cosmological collapse timescales, as we have discussed above. This happens because the cosmological collapse depends on realistic properties of DM halos, such as their shapes. In a more controlled environment of isolated models, GADGET-

3 exhibits earlier direct collapse than Enzo-2.4, due to the difference in the early force, mass and hydrodynamic resolution between the two codes.

In summary, we have performed a comparison between the AMR code Enzo-2.4 and the SPH code GADGET-3 in the framework of direct collapse to SMBH seeds, using both isolated and fully cosmological models of the collapse. We have followed the model evolution into a strongly nonlinear regime, when small initial differences have been substantially amplified. Although the overall model evolution has been found similar at large, substantial differences also exist at the end of the runs. We find that the main cause for these differences lies in different evolutionary pace of mass and spatial resolution with time and space. This results in different abilities of the numerical schemes to resolve hydrodynamics and gravitational interactions, such as shocks and angular momentum transfer by gravitational torques.

## ACKNOWLEDGMENTS

We thank the Enzo and YT support team for help. All analysis has been conducted using YT (Turk et al. 2011, <http://yt-project.org/>). We have used the Grackle chemistry and cooling library (Bryan et al. 2014b; Kim et al. 2014, <https://grackle.readthedocs.org/>). We are grateful to Volker Springel for providing us with the original version of GADGET-3, and to Jun-Hwan Choi and Long Do Cao for their help in the early phase of this project. K.N. acknowledges the partial support by JSPS KAKENHI Grant Number 26247022. I.S. acknowledges partial support from STScI grant AR-12639.01-A. I.S. and K.N. are grateful to the support from the International Joint Research Promotion Program at Osaka University. Support for HST/STScI AR-12639.01-A was provided by NASA through a grant from the STScI, which is operated by the AURA, Inc., under NASA contract NAS5-26555. Numerical simulations were in part carried out on XC30 at the Center for Computational Astrophysics, National Astronomical Observatory of Japan, as well as the VCC at the Cybermedia Center at Osaka University.

## REFERENCES

- Abel T., Anninos P., Zhang Y., Norman M. L., 1997, *New Astronomy*, 2, 181
- Abel T., Bryan G. L., Norman M. L., 2002, *Science*, 295, 93
- Agertz O., Moore B., Stadel J., Potter D., Miniati F., Read J., Mayer L., Gawryszczak A., Kravtsov A., Nordlund Å., Pearce F., Quilis V., Rudd D., Springel V., Stone J., Tasker E., Teyssier R., Wadsley J., Walder R., 2007, *MNRAS*, 380, 963
- Anninos P., Zhang Y., Abel T., Norman M. L., 1997, *New Astronomy*, 2, 209
- Ascasibar Y., Yepes G., Müller V., Gottlöber S., 2003, *MNRAS*, 346, 731
- Balsara D. S., 1995, *Journal of Computational Physics*, 121, 357
- Barnes J., Hut P., 1986, *Nature*, 324, 446
- Bate M. R., Burkert A., 1997, *MNRAS*, 288, 1060

- Begelman M. C., Rees M. J., 1978, *MNRAS*, 185, 847
- Begelman M. C., Rossi E. M., Armitage P. J., 2008, *MNRAS*, 387, 1649
- Begelman M. C., Shlosman I., 2009, *ApJL*, 702, L5
- Begelman M. C., Volonteri M., Rees M. J., 2006, *MNRAS*, 370, 289
- Berger M. J., Colella P., 1989, *Journal of Computational Physics*, 82, 64
- Bromm V., 2013, *Reports on Progress in Physics*, 76, 112901
- Bromm V., Larson R. B., 2004, *ARA&A*, 42, 79
- Bromm V., Loeb A., 2003, *ApJ*, 596, 34
- Bryan G. L., Norman M. L., 1997, in *Astronomical Society of the Pacific Conference Series*, Vol. 123, *Computational Astrophysics; 12th Kingston Meeting on Theoretical Astrophysics*, Clarke D. A., West M. J., eds., p. 363
- Bryan G. L., Norman M. L., O'Shea B. W., Abel T., Wise J. H., Turk M. J., Reynolds D. R., Collins D. C., Wang P., Skillman S. W., Smith B., Harkness R. P., Bordner J., Kim J.-h., Kuhlen M., Xu H., Goldbaum N., Hummels C., Kritsuk A. G., Tasker E., Skory S., Simpson C. M., Hahn O., Oishi J. S., So G. C., Zhao F., Cen R., Li Y., Enzo Collaboration, 2014a, *ApJS*, 211, 19
- , 2014b, *ApJS*, 211, 19
- Bryan G. L., Norman M. L., Stone J. M., Cen R., Ostriker J. P., 1995, *Computer Physics Communications*, 89, 149
- Bullock J. S., Dekel A., Kolatt T. S., Kravtsov A. V., Klypin A. A., Porciani C., Primack J. R., 2001, *ApJ*, 555, 240
- Choi J.-H., Shlosman I., Begelman M. C., 2013, *ApJ*, 774, 149
- , 2015, *MNRAS*, 450, 4411
- Colella P., Woodward P. R., 1984, *Journal of Computational Physics*, 54, 174
- Cullen L., Dehnen W., 2010, *MNRAS*, 408, 669
- Eisenstein D. J., Hut P., 1998, *ApJ*, 498, 137
- Ferland G. J., Porter R. L., van Hoof P. A. M., Williams R. J. R., Abel N. P., Lykins M. L., Shaw G., Henney W. J., Stancil P. C., 2013, *Rev. Mex. de Astronom. y Astrof.*, 49, 137
- Fraser M., Casey A. R., Gilmore G., Heger A., Chan C., 2015, *ArXiv:1511.03428*
- Frenk C. S., White S. D. M., Bode P., Bond J. R., Bryan G. L., Cen R., Couchman H. M. P., Evrard A. E., Gnedin N., Jenkins A., Khokhlov A. M., Klypin A., Navarro J. F., Norman M. L., Ostriker J. P., Owen J. M., Pearce F. R., Pen U.-L., Steinmetz M., Thomas P. A., Villumsen J. V., Wadsley J. W., Warren M. S., Xu G., Yepes G., 1999, *ApJ*, 525, 554
- Haehnelt M. G., Rees M. J., 1993, *MNRAS*, 263, 168
- Hahn O., Abel T., 2011, *MNRAS*, 415, 2101
- Heller C. H., Shlosman I., 1994, *ApJ*, 424, 84
- Hirano S., Hosokawa T., Yoshida N., Umeda H., Omukai K., Chiaki G., Yorke H. W., 2014, *ApJ*, 781, 60
- Hopkins P. F., 2013, *MNRAS*, 428, 2840
- Hosokawa T., Omukai K., Yoshida N., Yorke H. W., 2011, *Science*, 334, 1250
- Inayoshi K., Omukai K., Tasker E., 2014, *MNRAS*, 445, L109
- Jappsen A.-K., Mac Low M.-M., Glover S. C. O., Klessen R. S., Kitsionas S., 2009, *ApJ*, 694, 1161
- Johnson J. L., Khochfar S., Greif T. H., Durier F., 2011, *MNRAS*, 410, 919
- Kim J.-H., Abel T., Agertz O., Bryan G. L., Ceverino D., Christensen C., Conroy C., Dekel A., Gnedin N. Y., Goldbaum N. J., Guedes J., Hahn O., Hobbs A., Hopkins P. F., Hummels C. B., Iannuzzi F., Keres D., Klypin A., Kravtsov A. V., Krumholz M. R., Kuhlen M., Leitner S. N., Madau P., Mayer L., Moody C. E., Nagamine K., Norman M. L., Onorbe J., O'Shea B. W., Pillepich A., Primack J. R., Quinn T., Read J. I., Robertson B. E., Rocha M., Rudd D. H., Shen S., Smith B. D., Szalay A. S., Teyssier R., Thompson R., Todoroki K., Turk M. J., Wadsley J. W., Wise J. H., Zolotov A., AGORA Collaboration, 2014, *ApJS*, 210, 14
- Komatsu E., Dunkley J., Nolte M. R., Bennett C. L., Gold B., Hinshaw G., Jarosik N., Larson D., Limon M., Page L., Spergel D. N., Halpern M., Hill R. S., Kogut A., Meyer S. S., Tucker G. S., Weiland J. L., Wollack E., Wright E. L., 2009, *ApJS*, 180, 330
- Koushiappas S. M., Bullock J. S., Dekel A., 2004, *MNRAS*, 354, 292
- Kravtsov A. V., Klypin A. A., Khokhlov A. M., 1997, *ApJS*, 111, 73
- Larson R. B., 1969, *MNRAS*, 145, 405
- Latif M. A., Schleicher D. R. G., Schmidt W., Niemeyer J., 2013, *MNRAS*, 433, 1607
- Latif M. A., Zaroubi S., Spaans M., 2011, *MNRAS*, 411, 1659
- Loeb A., Rasio F. A., 1994, *ApJ*, 432, 52
- Long S., Shlosman I., Heller C., 2014, *ApJL*, 783, L18
- Madau P., Rees M. J., 2001, *ApJL*, 551, L27
- Mayer L., Kazantzidis S., Escala A., Callegari S., 2010, *Nature*, 466, 1082
- Milosavljević M., Bromm V., Couch S. M., Oh S. P., 2009, *ApJ*, 698, 766
- Navarro J. F., Frenk C. S., White S. D. M., 1997, *ApJ*, 490, 493
- Norman M. L., Bryan G. L., 1999, in *Astrophysics and Space Science Library*, Vol. 240, *Numerical Astrophysics*, Miyama S. M., Tomisaka K., Hanawa T., eds., p. 19
- Omukai K., 2001, *ApJ*, 546, 635
- O'Shea B. W., Nagamine K., Springel V., Hernquist L., Norman M. L., 2005, *ApJS*, 160, 1
- Penston M. V., 1969, *MNRAS*, 144, 425
- Price D. J., Federrath C., 2010, *MNRAS*, 406, 1659
- Prieto J., Jimenez R., Haiman Z., 2013, *MNRAS*, 436, 2301
- Saitoh T. R., Makino J., 2013, *ApJ*, 768, 44
- Schleicher D. R. G., Spaans M., Glover S. C. O., 2010, *ApJL*, 712, L69
- Shapiro S. L., Teukolsky S. A., 1985, *ApJ*, 298, 58
- Shlosman I., Choi J.-H., Begelman M. C., Nagamine K., 2016, *MNRAS*, 456, 500
- Springel V., 2005, *MNRAS*, 364, 1105
- Springel V., Hernquist L., 2003, *MNRAS*, 339, 289
- Sugimura K., Omukai K., Inoue A. K., 2014, *MNRAS*, 445, 544
- Tasker E. J., Brunino R., Mitchell N. L., Michielsen D., Hopton S., Pearce F. R., Bryan G. L., Theuns T., 2008, *MNRAS*, 390, 1267
- Truelove J. K., Klein R. I., McKee C. F., Holliman II J. H., Howell L. H., Greenough J. A., 1997, *ApJL*, 489, L179
- Turk M. J., Abel T., O'Shea B., 2009, *Science*, 325, 601
- Turk M. J., Smith B. D., Oishi J. S., Skory S., Skillman

- S. W., Abel T., Norman M. L., 2011, *ApJS*, 192, 9  
Vogelsberger M., Sijacki D., Kereš D., Springel V., Hernquist L., 2012, *MNRAS*, 425, 3024  
Volonteri M., Rees M. J., 2005, *ApJ*, 633, 624  
—, 2006, *ApJ*, 650, 669  
Wise J. H., Abel T., Turk M. J., Norman M. L., Smith B. D., 2012, *MNRAS*, 427, 311  
Zel’dovich Y. B., Podurets M. A., 1965, *Astron.Zh.*, 42, 963